NSF Grant UM#02-522627
National Science Foundation

EVALUATING THE USE OF POLARIMETRIC CLOUD RADARS FOR STUDYING WINTER STORMS

by David A. Long and Steven A. Rutledge

Colorado
State
University

DEPARTMENT OF
ATMOSPHERIC SCIENCE

PAPER NO. 748

EVALUATING THE USE OF POLARIMETRIC CLOUD RADARS FOR STUDYING WINTER STORMS

by

David A. Long

and

Steven A. Rutledge

Department of Atmospheric Science

Colorado State University

Fort Collins, CO 80523

Research Supported by

National Science Foundation

under Grant UM#02-522627

Spring 2004

Atmospheric Science Paper No. 748

ABSTRACT

EVALUATING THE USE OF POLARIMETRIC CLOUD RADARS FOR STUDYING WINTER STORMS

The purpose of this research was to model two Front Range snowstorms at millimeter wavelengths in order to evaluate the performance of the millimeter wavelengths concerning storm microphysics. Specifically, the question at what point, if any, do Mie scattering effects and attenuation become detrimental to further analysis is addressed. The T-matrix method was used to model the storms at Ku-band, Ka-band, and W-band: these wavelengths were chosen to simulate the Advanced Multi-Frequency Radar (AMFR), which is currently being developed by the University of Massachusetts in collaboration with CSU. The AMFR includes full polarimetric capability, so the modeled results include Z_h as well as polarimetric quantities.

The two snowstorms chosen were the March 2003 snowstorm and the October 1997 blizzard. Hydrometeor identification by means of fuzzy logic was used on the March 2003 snowstorm to extract microphysical information from the CHILL images to use as input for the T-matrix model. At 0600 UTC on 18 March 2003, the hydrometeor identification revealed a bright band east of about 30 km west of CHILL, where a barrier jet was located at the time. Snow was observed falling to the ground west of this boundary. At 0000 UTC on 19 March 2003, the storm was much more stratified, with snow falling everywhere in the radar domain. Modeled results for the earlier time indicate the oscillatory nature of the Mie regime when Z_h for rain is examined, where Z_h is 35.0

dBZ at S-band and 35.1 dBZ at Ku-band. The model output for a rain/snow mix was almost identical to that of rain alone, the dominant dielectric. For 0000 UTC on 19 March 2003, it was found that changing the density and particle size distributions of snow aggregates and crystals greatly affected the model output. Model output at both times displayed consistent trends such as low Z_h (due to Mie scattering) and higher attenuation at the shorter wavelengths.

Microphysical information for the October 1997 blizzard was generated by the CSU-RAMS model, and this output was then used as input into T-matrix. Output (polarimetric radar quantities) was compared to CHILL images to verify the physical reality of the RAMS output. Output images from the T-matrix model indicated strong Mie effects at Ka-band and especially W-band. Z_h was reduced to below 0 dBZ at W-band due to strong Mie scattering and path-dependent attenuation. The signal loss and oscillatory backscattering cross sections of the hydrometeors at W-band was detrimental to the interpretation of the other polarimetric quantities, and little physical interpretation could be done. It was concluded that Ku-band could be a useful observational wavelength, while Ka-band and W-band may not be useful in observing intense winter storms.

ACKNOWLEDGEMENTS

We would like to thank Drs. William Cotton and V. Chandrasekar for their willingness to serve on Mr. Long's committee and their input on this work. We are grateful to the CSU radar meteorology group for helpful discussions pertaining to this research. Specifically, we would like to thank Tracy Depue, Brenda Dolan, and Kyoko Ikeda for frequent conversation. Also, thanks to Kyle Wiens for his fuzzy logic computer program and the mbf's generated from it. Thanks to Sarah Tessendorf and Gustavo Pereira for their suggestions on writing this thesis, and to Margi Cech for her support during Mr. Long's time at CSU. Paul Hein spent much time helping with computer programming in general and in this research and his efforts are greatly appreciated. We are grateful to Drs. Larry Carey and Walt Petersen for their help and guidance with the T-matrix program, and to Dr. Andrew Heymsfield and Pat Kennedy for valuable discussions pertaining to the microphysics of snow. Drs. Rob Cifelli, Steve Nesbitt, and Tim Lang participated in insightful discussions with us. Thanks to Steve Saleeby and Ray McAnelly for retrieving the necessary RAMS files for this research. This research was supported by the National Science Foundation, through subcontract UM# 02-522627 A 02 with the University of Massachusetts.

TABLE OF CONTENTS

LIST OF TABLES

LIST OF FIGURES

Chapter 1

INTRODUCTION

Radars in the field of meteorology have been traditionally used for observation of precipitation. Doppler radar can measure the relative movement of the precipitation towards or away from the radar, and polarimetric radar can calculate parameters based on the shape, phase, and fall mode of hydrometeors. This ability of polarimetric radars makes them useful in microphysical analyses. The National Weather Service's WSR-88D radars are a nationwide network of Doppler radars that measure precipitation coverage and intensity, as well as provide information on storm and clear air wind patterns. The CSU-CHILL radar is a polarimetric Doppler radar that can directly observe particle shape in addition to the functions of traditional Doppler radar. One property that all of these radars and, in fact, most of the weather radars in use today share is that they all transmit electromagnetic radiation at centimeter wavelengths. The CSU-CHILL radar and the WSR-88D network are S-band radars, meaning that the transmitted radiation has approximately a 10 cm wavelength. C-band, X-band, and Ku-band are the other centimeter wavelengths used in the weather radar spectrum. C-band radars operate at wavelengths around 5 cm, and X-band radars have wavelengths near 3 cm. At these wavelengths, smaller antennas mean smaller, more portable radars. In situations where size is an issue, such as mobile radars for storm chasing, C and X-band radars are used.

Millimeter wavelength radars have been developed and used for research in the atmospheric science community, especially over the last 10 years. The purpose behind developing radars at these short wavelengths is both scientific and economical. Given that C and X-band radars are smaller than S-band radars, millimeter radars are even more portable. Smaller antennas and less powerful transmitters can be used at millimeter wavelengths to achieve similar sensitivities, and this is attractive economically. Also, millimeter radars can "see" clouds in more detail than centimeter radars. The theory behind this will be addressed in Chapter 2. Cloud studies are at the cutting-edge of research in the atmospheric sciences due to their role in the earth's radiation budget. Despite these advantages of millimeter wavelength radars over centimeter wavelength radars, tradeoffs are always the rule. Attenuation, which will also be discussed in detail in Chapter 2, becomes more problematic at shorter radar wavelengths. Also, the Rayleigh approximation for scattering is often not applicable for millimeter wavelengths observing precipitation, where Mie scattering can often be dominant. For these reasons, millimeter radars can suffer severe or complete loss of signal depending on the specific radar wavelength and the intensity of precipitation they observe.

The University of Massachusetts, in collaboration with CSU, is currently developing a multi-frequency polarimetric millimeter radar known as the Advanced Multi-Frequency Radar, or AMFR. This study attempts to model the precipitation structure in two winter storms along the Front Range of Colorado using the AMFR wavelengths. Since AMFR is in the process of being built, the storms will be modeled at these frequencies using microphysical data from the winter storms observed by the CSU-CHILL radar. The two major winter storms that were studied are: The October 1997 blizzard and the March 2003 snowstorm. In both cases, the CSU-CHILL radar observed the winter storms at S-band. Since snow attenuates the radar signal significantly less than rain, it is hopeful that these storms can be observed meaningfully at millimeter wavelengths. It is important to determine at what wavelength, if any, these storms or storms of similar intensity are observed too poorly at millimeter wavelengths to offer any scientific information or operational possibility. The purpose of this study is to model two winter storms at millimeter wavelengths in order to evaluate the usefulness in observing the microphysical structure of winter storms at these wavelengths. Observed microphysical information will be used as input into a scattering model that calculates various radar meteorology quantities, including polarimetric variables.

Chapter 2

BACKGROUND AND METHODS

2.1 Polarimetric Radar Variables

The CSU-CHILL S-band (λ=11cm) radar was used in this study as the observational radar for both storms: the March 2003 snowstorm and the October 1997 blizzard. CHILL is a polarimetric radar, meaning that it can transmit and receive electromagnetic waves in both a horizontal and vertical orientation (Figure 2.1). Unlike the WSR-88D radars that can only measure horizontal reflectivity and radial velocity, CHILL receives information from the backscattered radiation pertaining to particle shape, orientation, phase, and fall mode.

2.1.1 Reflectivity

All weather radars can measure the backscattered power, or reflectivity, of a radar volume. Assuming that the scatterers in the radar volume are in the Rayleigh regime, meaning that the diameters of the hydrometeors are sufficiently small compared to the wavelength of the radar wave, the reflectivity factor is defined as:

$$Z_e = \int_0^\infty N(D) D^6 dD \tag{2.1}$$

Z_e, in units of mm^6 m^{-3}, is the total backscattered power in a radar volume and depends on particle diameter to the sixth power. It is clear from Eq. 2.1 that larger particles dominate the reflectivity. Since Z_e can vary from 0.001 mm^6 m^{-3} in fog to 10^7 mm^6 m^{-3} with softball size hail, a logarithmic scale must be used (Rinehart, 1997). This form of the reflectivity factor can be expressed as:

$$dBZ = 10\log_{10}(Z_e) \tag{2.2}$$

Since it is customary to measure reflectivity with the horizontally polarized wave, the horizontal reflectivity (Z_h) is used to measure the total backscattered power in a radar volume. Z_h typically varies at S-band from 0 dBZ for cumulus clouds to 30 dBZ for heavy snow to 65 dBZ or more for large hail.

2.1.2 Radial velocity

Doppler radars can measure the frequency shift of a moving weather target. This is known as the radial velocity (V_r), which is the movement of hydrometeors toward or away from the radar. V_r can be useful in measuring the speed of straight-line winds from a bow echo or the speed of the rotating winds from a tornado. In winter storms along the Front Range, it is useful for determining the depth of upslope winds, which are crucial for the development of widespread precipitation.

2.1.3 Differential reflectivity

Differential reflectivity (Z_{dr}), in units of dB, is defined as follows:

$$Z_{dr} = 10\log_{10}\left(\frac{Z_{hh}}{Z_{vv}}\right) \tag{2.3}$$

where Z_{hh} is the co-polar received power for horizontal polarization, and Z_{vv} is the co-polar received power for vertical polarization. Notice that Z_{dr} is the first polarimetric variable discussed, because conventional radars can transmit and receive electromagnetic waves in only one plane, usually horizontal. The co-polar signal is when the radar transmits and receives radiation in the same plane: Z_{dr} calculates the ratio of the horizontal and vertical co-polar signals on a logarithmic scale. Z_{dr} gives a measure of the prolateness ($-Z_{dr}$) or oblateness ($+Z_{dr}$) of a hydrometeor. While negative Z_{dr}'s are possibly associated with large hail, snow aggregates tend to have a near zero or slightly positive Z_{dr} while plate-like snow crystals would have a larger Z_{dr} (Lhermitte, 1990). Rain returns increasingly positive Z_{dr} with increasing size. Since Z_{dr} contains information about the shape of a particle, it is often used to distinguish intense rainfall (positive Z_{dr}'s) from hail (Z_{dr}'s around 0).

2.1.4 Linear depolarization ratio

The linear depolarization ratio (LDR) is defined as:

$$LDR = 10\log_{10}\left(\frac{Z_{hv}}{Z_{hh}}\right) \tag{2.4}$$

where Z_{hv} is known as the cross-polar signal. This signal is much weaker than the co-polar signal and has contributions from particle shape asymmetries and the distribution of canting angles, or amount of wobbling, of falling hydrometeors. Large, irregular-shaped hail has the greatest LDR's associated with it, because its tumbling nature and irregular shape return a relatively large cross-polar signal (i.e., depolarize the incident radiation). LDR is on a logarithmic scale and has units of dB.

2.1.5 *Specific differential phase*

Specific differential phase (K_{dp}) is not directly measured by the radar. It is derived from ϕ_{dp}, the differential propagation phase. ϕ_{dp} is the phase shift between horizontal and vertical radiation due to oblate-shaped hydrometeors. K_{dp} is calculated by taking ½ $d\phi_{dp}/dr$, where r is range. It is affected only by anisotropic scatterers, such as rain, because isotropic scatterers produce equal phase shifts in horizontal and vertical polarizations (Doviak and Zrnic, 1993). This makes K_{dp} useful in detecting the amount of rain in a rain/hail mix. K_{dp} is relatively unexplored at millimeter wavelengths.

2.1.6 *Correlation coefficient*

The correlation coefficient at zero time lag ($\rho_{hv}(0)$) uses the horizontally and vertically polarized waves that are received at the closest time from each other. ρ_{hv} depends on the shape, oscillation, wobbling, and canting angle distribution of hydrometeors (Doviak and Zrnic, 1993). Consequently, mixed phase volumes are more decorrelated, because each hydrometeor type has a different shape and canting angle distribution. This results in a lowering of ρ_{hv} from values slightly less than unity.

2.2 Millimeter Wavelength Radar

2.2.1 Comparison of Ku, Ka, and W-band to S-band

The Advanced Multi-Frequency Radar (AMFR) has three wavelengths: Ku-band, with frequency of 13.8 GHz corresponding to a wavelength of 2.2 cm, Ka-band, with a frequency of 33 GHz corresponding to a wavelength of 8.4 mm, and W-band, with a frequency of 95 GHz corresponding to a wavelength of 3.2 mm. Strictly speaking, Ku-band is a centimeter wavelength, but it is grouped with Ka-band and W-band to form AMFR, mainly to provide a frequency match to the precipitation radar on TRMM. The wavelengths of the AMFR were chosen to reduce the impact of absorption of the radar wave by gases in the atmosphere such as oxygen and water vapor (Lhermitte, 1990). These wavelengths are primarily used in the remote sensing of clouds droplets and light precipitation. Since the backscattering cross section of these cloud droplets goes as $1/\lambda^4$ using the Rayleigh approximation, millimeter radars are more sensitive than S-band for a given transmit power. However, this study involves precipitation-sized particles such as rain and snow, and the Rayleigh approximation becomes invalid at the shorter wavelengths where Mie scattering dominates. Within the Mie regime, the backscattering cross section of particles decreases from that of the Rayleigh approximation due to increased forward scattering. It is also oscillatory, meaning that an increase in particle size may increase or decrease its backscattering cross section; obviously, scattering effects are more complicated in the Mie regime, especially with snow due to its irregular shape. In Chapters 3 and 4, this behavior will be manifest in modeled polarimetric quantities that are difficult to interpret at the shorter wavelengths. Table 2.1 shows the maximum particle diameter for Rayleigh scattering for each hydrometeor modeled in this study at each wavelength.

The results for this study (for the particular cases that were examined) are that all modeled hydrometeors are Rayleigh scatterers at S-band. At Ku-band, the smaller raindrops and aggregates and all of the snow crystals are still Rayleigh scatterers while the larger raindrops and aggregates are now Mie scatterers. At Ka-band, all of the raindrops and most of the aggregates are in the Mie regime, while most of the snow crystals are still in the Rayleigh regime. At W-band, all of the particles are Mie scatterers except for the smallest snow crystals. From this, it is clear that the shorter the radar wavelength is, the more effect that Mie scattering has on the radar measurements.

2.2.2 *Advantages and disadvantages of millimeter radars*

There are both advantages and disadvantages to using millimeter radars when compared to S-band radars. As previously mentioned, millimeter radars are more sensitive cloud radars; however, this study models precipitation-sized particles, so this advantage may not always be a factor. The other main advantage is an economical one: very narrow beams with a small antenna and a low power transmitter (Lhermitte, 1990). In other words, a 1° beam can be achieved at millimeter wavelengths with a much smaller antenna. This means that millimeter radars are more portable and more affordable.

In addition to severely diminished backscattering cross sections and oscillatory backscattering cross sections of hydrometeors deep within the Mie regime, a major disadvantage of millimeter radars is attenuation. The extinction cross section is given as:

$$Q_{ext} = Q_a + Q_s \qquad (2.5)$$

The scattering cross section (Q_s) plus the absorption cross section (the dissipation of electromagnetic energy in the form of heat; Q_a) constitute the extinction cross section, which is related to attenuation along the path of the radar beam (Lhermitte, 2002). As more of the particles along the path of the radar beam become Mie scatterers, more of the incident radiation is scattered away in directions other than back toward the radar. This effect can be quantified as Q_s (Lhermitte, 2002). The scattering cross section is negligible for raindrops in the Rayleigh regime, but it becomes significant when these raindrops transition to Mie scatterers. Figure 2.2 illustrates the relative contributions of Q_a and Q_s to Q_{ext} for rain at W-band. Since winter storms are composed of snow, which has a weaker dielectric response than rain, and because they are observed at lower reflectivities than thunderstorms or even moderate rain most of the time, perhaps a millimeter radar would be able to measure a snowstorm without suffering too much signal loss due to Mie effects and/or path dependent attenuation (Battan, 1973; Lhermitte, 2002). The point of this work is to see how much signal loss is observed during intense winter storms and, consequently, determining the point, if any, that signal loss is detrimental to the observed structure of the storm.

2.3 Hydrometeor Identification Using Fuzzy Logic

For the March 2003 snowstorm, hydrometeor identification by means of fuzzy logic was performed on the CSU-CHILL radar images in order partition these images into hydrometeor type (Liu and Chandrasekar, 2000). This was the first step in modeling the storm.

Before fuzzy logic was used, the data needed to be edited and transformed to a Cartesian grid. Software written by Dr. Lawrence Carry was used to calculate K_{dp} from

ϕ_{dp} and to remove noise and ground clutter from the radar images in Universal Format (.uf). The software calculated K_{dp} by taking the range derivative of ϕ_{dp}, directly measured by the radar. Noise and ground clutter were removed by setting the ρ_{hv} threshold to 0.8; this effectively flags any gate of data that has a ρ_{hv} value of less than 0.8, and the corresponding gates in all of the fields are deleted. Each radar image in Universal Format was then transformed into a Cartesian grid (.cdf file) using REORDER, software written by NCAR. The Cressman weighting scheme was used to grid the data using a horizontal resolution of 0.5 km and a vertical resolution of 0.35 km. The radius of influence, which is the ellipsoid that sets the boundaries of the data used to calculate the corresponding grid point, had an azimuth of 1.2° and an elevation of 1.0°. A smaller radius of influence would generate a higher resolution grid, while a larger one would "smooth" the data to a higher degree.

2.3.1 Fuzzy logic

Hydrometeor identification is simply a means of classifying hydrometeor type using polarimetric quantities, and fuzzy logic is the method used for hydrometeor identification. The "fuzzy" boundaries inherent in the polarimetric quantities that describe a particle can be used in the fuzzy logic method, and this reasoning can be found in Vivekanandan et al. (1999). Fuzzy logic is a weighted sum in which the hydrometeor type with the highest score is assigned to the particle. This score is derived from the membership beta functions (mbf's), in which each polarimetric quantity is assigned a probability between 0 and 1 for each hydrometer. To illustrate, consider snow described by Z_h. A reflectivity of 20 dBZ would be assigned a value of 1, while a reflectivity of 60 dBZ would be assigned a value of 0. A reflectivity of 36 dBZ may be assigned a value somewhere between 0 and 1. Because of the smooth transitions between hydrometeor types, a point with a Z_h of 36 dBZ would not necessarily be eliminated as being snow. This first step of converting the particle in question to mbf's and placing them in fuzzy sets according to hydrometeor type is called "fuzzification" (Liu and Chandrasekar, 2000). The second step is called "inference", and this combines the truth-value of each mbf to get a combined truth-value for each fuzzy set. The third step is termed "aggregation", which finds the fuzzy set with the maximum truth-value. The fourth step, "defuzzification", outputs the hydrometeor type. Figure 2.3 shows a flow chart of this process.

2.3.2 *Fuzzy logic applied to the March 2003 snowstorm*

For simplicity, four hydrometeor types were chosen as possible outcomes using fuzzy logic: rain, drizzle, snow aggregates, and pristine (snow) crystals. For the membership beta functions (mbf's), Z_h, Z_{dr}, and temperature were used in the computation of the four possible hydrometeors. The temperature profile, except for the surface temperature, was retrieved from the Eta model analysis files for 1200 UTC, so the temperatures are model derived. The surface temperature was observed at approximately 40 km west of CHILL, and each temperature level was assumed to be uniform in that layer. Other polarimetric quantities were not used because it was found that Z_h, Z_{dr}, and temperature were adequate in constraining the possible hydrometeor type for this case study. For example, temperature alone can almost separate rain or drizzle from snow, although there is some overlap, and Z_{dr} can distinguish the flat, (assumed) dendritic crystals from the spherical-like snow aggregates. Z_h offers a loose barrier in that snow in any form usually does not exist above about 35-40 dBZ, so a score of 0 would be assigned to Z_h in the snow aggregate and crystal fuzzy sets for anything significantly over 35-40 dBZ (Straka et al., 2000; Lhermitte, 2002). Also, LDR, K_{dp}, and ρ_{hv} are very noisy at the lower reflectivities of winter storms and, consequently, can contaminate the results. Figures 2.4- 2.7 show the membership beta functions used for this case.

2.4 T-matrix Method of Modeling Hydrometeors

The Transition-matrix (T-matrix) and Mueller-matrix methods were used to model both storms, the March 2003 snowstorm and the October 1997 blizzard. These methods require microphysical information, such as particle shape, composition, and particle size distribution as input, and they calculate polarimetric quantities and attenuation, as well as other quantities, by essentially calculating the scattering behavior of a population of hydrometeors. The T-matrix computer program used (L. Carey, personal communication) applied theory concerning the T-matrix and the Mueller-matrix. The theory behind the T-matrix and Mueller-matrix codes will be addressed in the following paragraphs. The equations and a full treatment of the particle scattering problem and solutions can be found in Barber and Yeh (1975), which addresses the T-matrix method, and (Vivekanandan et al., 1991), which addresses the Mueller-matrix method.

The T-matrix method is used for calculating the theoretical scattering of nonspherical dielectric bodies (Barber and Yeh, 1975). It is especially suited for particles that are Mie scatterers, or particles on the order of the wavelength of the incident radiation. The T-matrix method introduced by Waterman (1969) uses the Extended Boundary Condition Method (EBCM) that produces a set of linear equations for the expansion coefficients of the scattered electromagnetic field in terms of the coefficients of the incident electromagnetic field. As stated in Barber and Yeh (1975) their approach first relates the internal fields (within the dielectric body) to the incident field, then relates the surface currents to the internal field, and lastly expresses the scattered field in terms of the surface currents.

The T-matrix method only calculates the scattering behavior of one dielectric body arbitrarily oriented in a laboratory setting. In order to describe the scattering of a radar volume that contains particles at different orientations and at different angles to the incident radar wave (radar elevation angle), the Mueller-matrix method is used (Vivekanandan et al., 1991). This method uses the procedure developed by Wang (1979) in which a coordinate system is added to the original T-matrix. This effectively rotates the incident and scattered waves and the unit vectors of the polarization states. The result is the 4 X 4 Mueller matrix. By rotating the directions of the EM waves and unit vectors, scattering behavior from any orientation can then be calculated by specifying a Gaussian fall mode and a radar elevation angle. All of the radar quantities, which depend on particle orientation, can then be calculated.

For both case studies, the same T-matrix code is used. When T-matrix is used in the following chapters, it really means the T-matrix and Mueller-matrix codes combined. The T-matrix and Mueller-matrix methods represent two different sets of code, in which the T-matrix output from the first code is used as input for the Mueller-matrix code. From the Mueller-matrix, the various radar quantities are calculated, specifically Z_h, Z_{dr}, LDR, K_{dp}, ρ_{hv}, and specific horizontal attenuation. As stated in Vivekanandan et al. (1991), the T-matrix is calculated once per particle shape, size, temperature, and dielectric constant. Once the T-matrix is calculated in the first code it, along with new inputs such as radar elevation angle and particle size distribution, are used as inputs for the Mueller-matrix code.

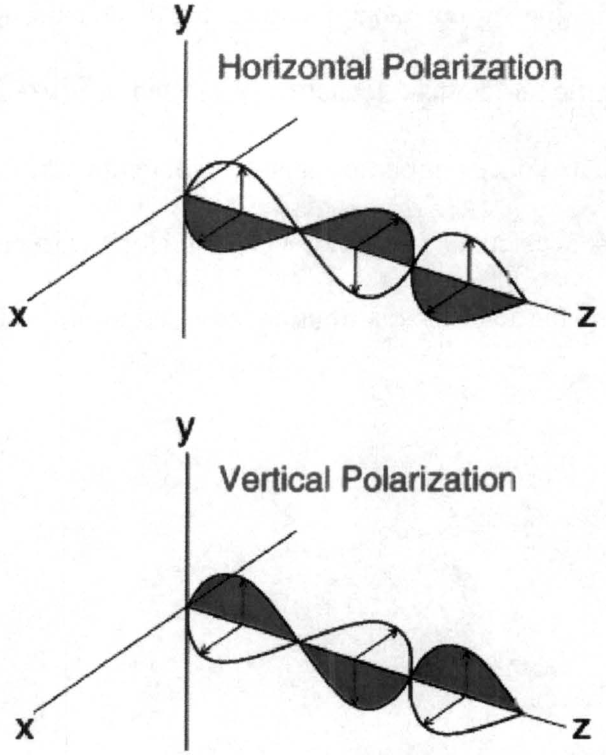

Figure 2.1: An illustration of a horizontally and vertically polarized electromagnetic wave. The blue shading and red shading represent the oscillating electric field within the horizontally and vertically oriented EM waves, respectfully, while the white shading represents the oscillating magnetic field in both orientations. Direction of propagation in both cases is along the z-axis (URL: http://cimms.ou.edu/~schuur/radar.html, 2004).

Table 2.1: Maximum particle diameter for Rayleigh scattering (D_{max}) for each hydrometeor at each wavelength.

Radar Wavelength (λ)	Rain	Snow Aggregates	Snow Crystals (Dendrites)
S-band (10 cm)	7.7 mm	1.69 cm	2.02 cm
Ku-band (2.2 cm)	1.5 mm	3.4 mm	4.1 mm
Ka-band (0.84 cm)	0.6 mm	1.3 mm	1.6 mm
W-band (0.32cm)	0.2 mm	0.5 mm	0.6 mm

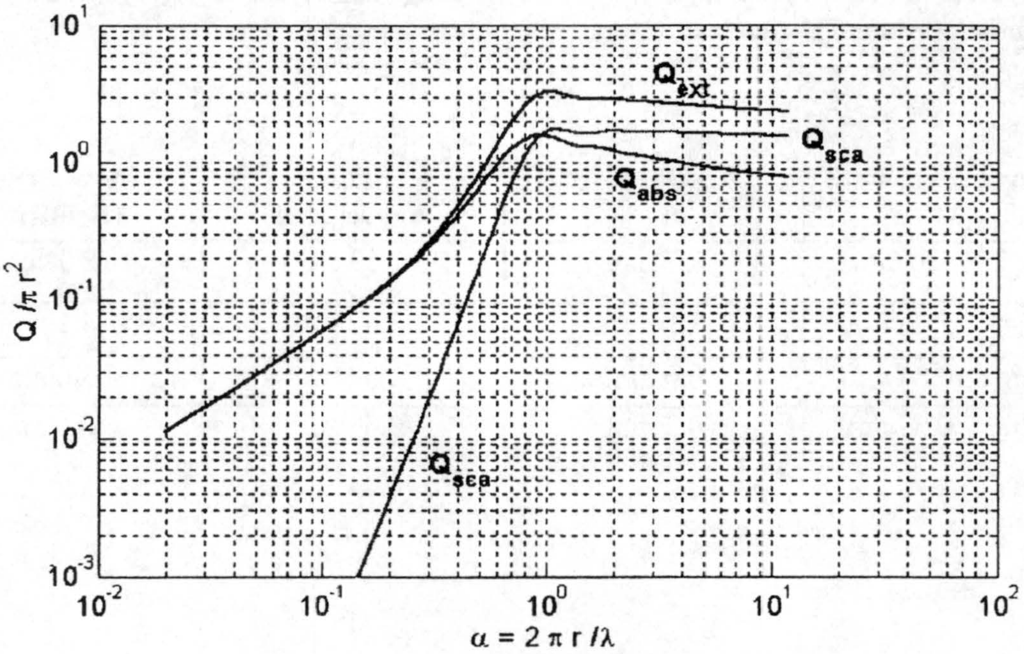

Figure 2.2: The extinction, absorption, and scattering cross sections as a function of the size parameter, α, for rain at 94 GHz (W-band) and 20°C. For a fixed wavelength (in this case, 3.2 mm), λ, a raindrop will transition from the Rayleigh regime at smaller r (drop radius) to the Mie regime at larger r. Notice the dramatic increase of the scattering cross section for rain as the drop transitions to the Mie regime (Lhermitte, 2002).

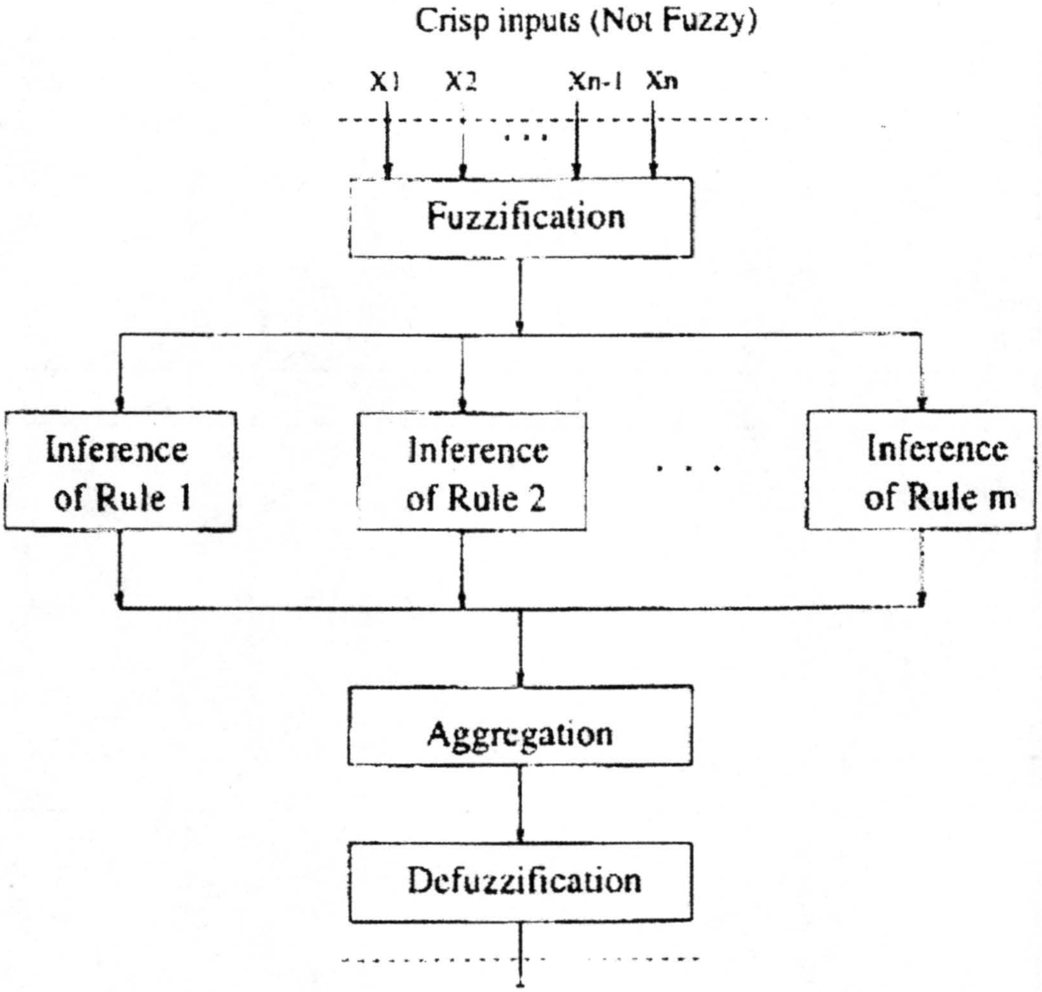

Figure 2.3: A schematic showing the fuzzy logic process. Crisp output is generated from "Defuzzification"(Liu and Chandrasekar, 2000).

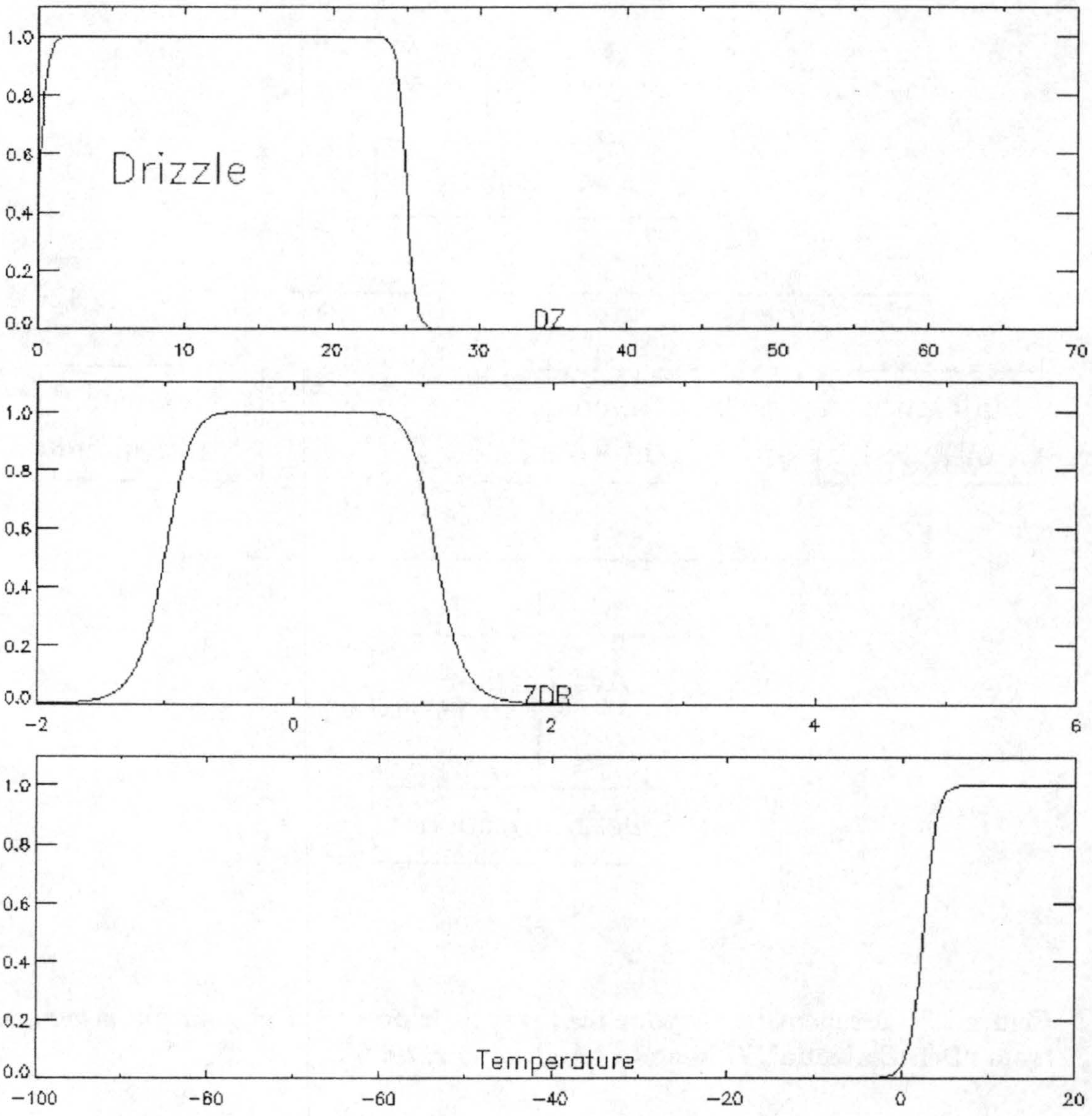

Figure 2.4: Membership beta functions for drizzle.

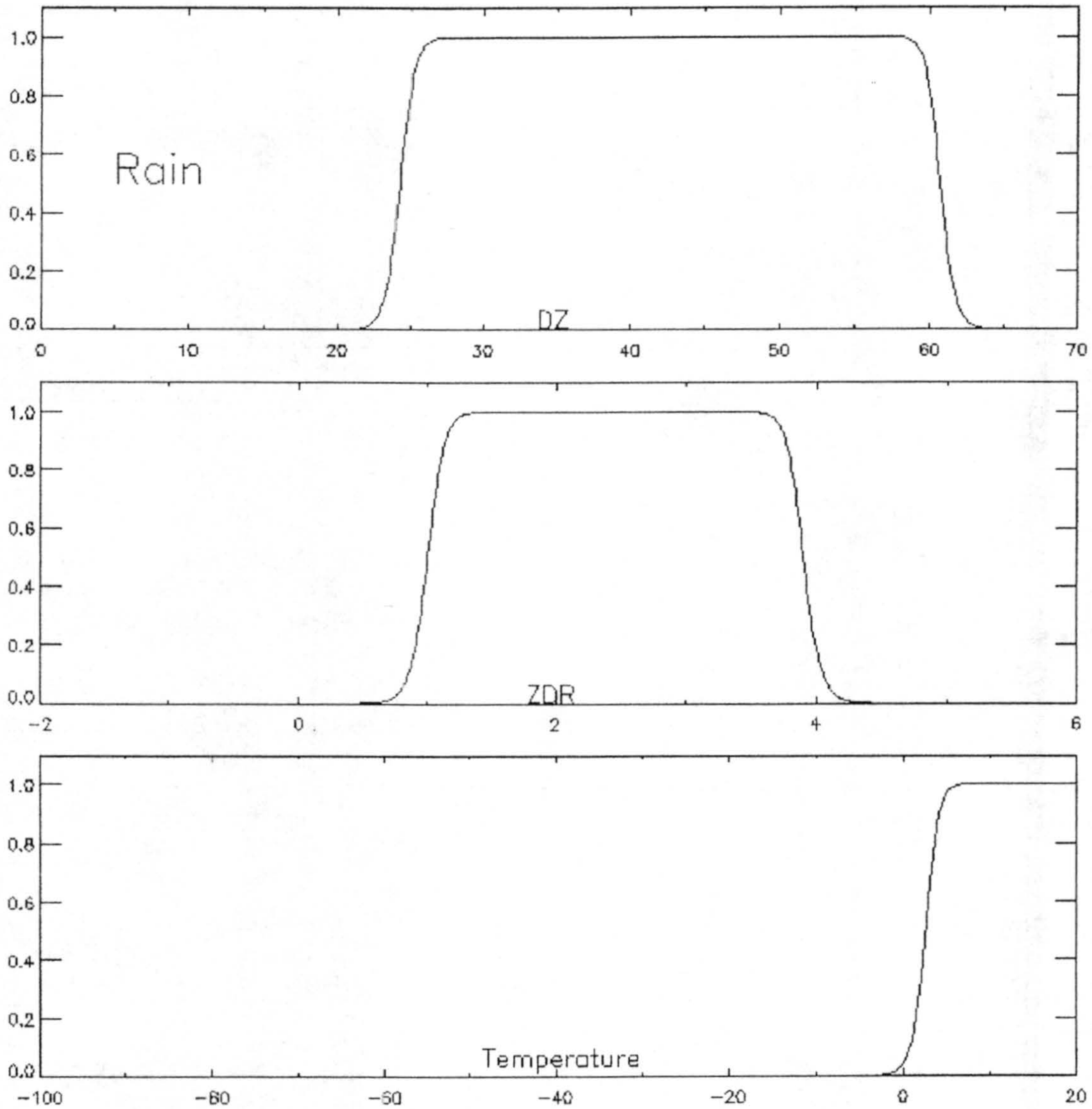

Figure 2.5: Membership beta functions for rain.

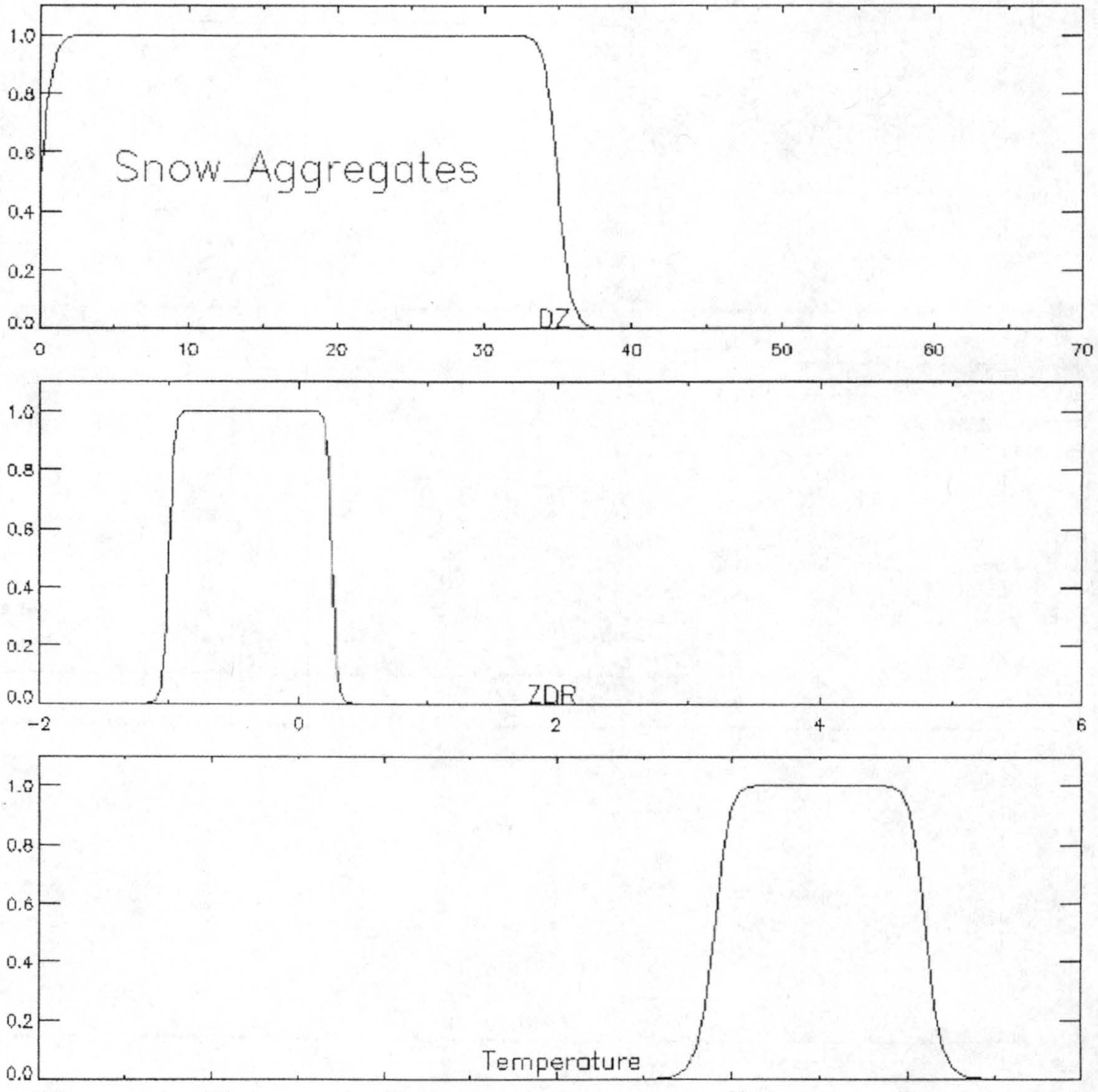

Figure 2.6: Membership beta functions for snow aggregates (snowflakes).

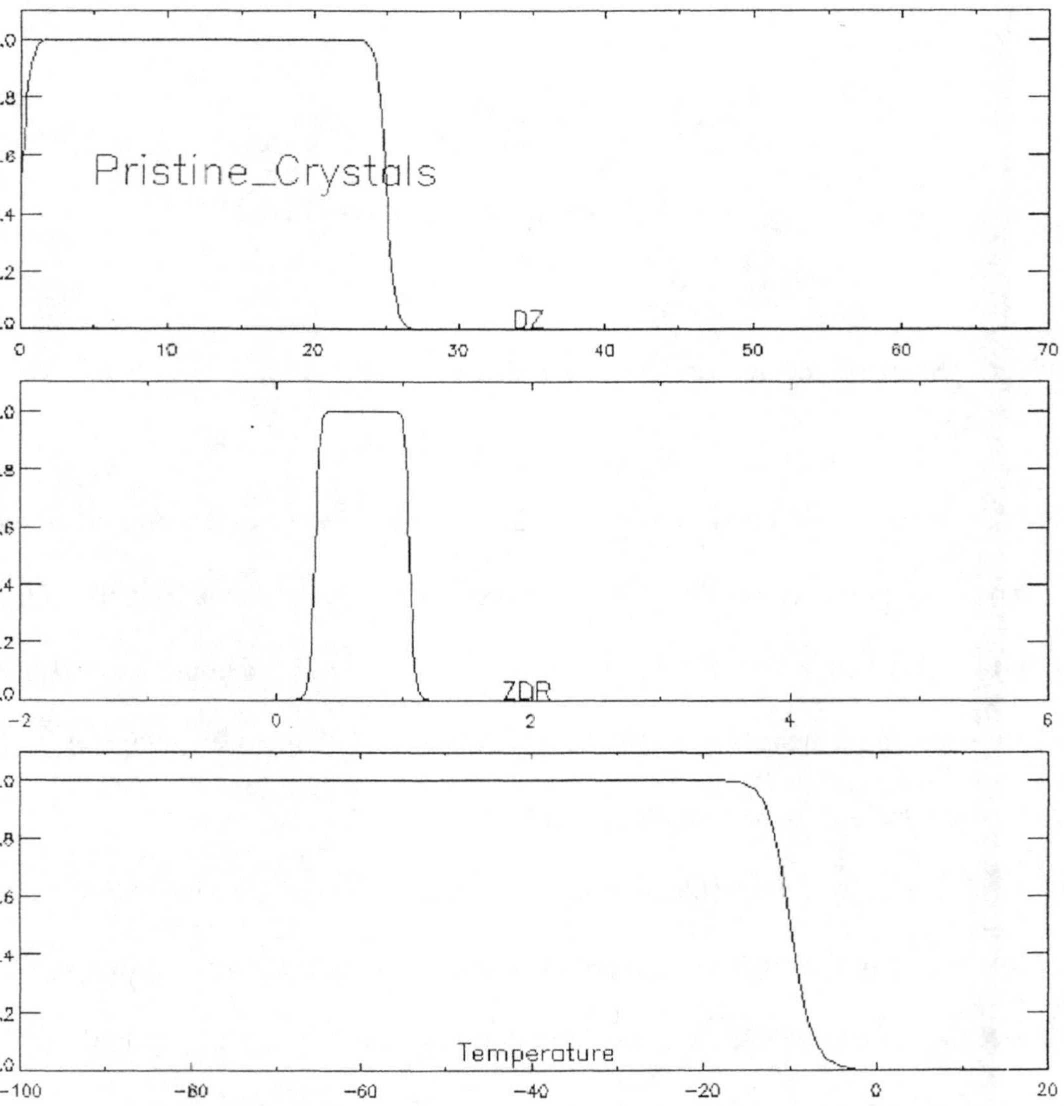

Figure 2.7: Membership beta functions for snow crystals (dendrites).

Chapter 3

THE MARCH 2003 SNOWSTORM

3.1 Storm Overview and Synoptic Environment

From 17 March to 19 March 2003, a historic winter storm produced record amounts of precipitation along the urban corridor and Front Range foothills of Colorado. Fort Collins received around 30 inches (66 cm) of snow with a liquid water equivalent between 5 and 6 inches (11 and 13.2 cm). Total snowfall approached 90 inches (198 cm) in some locations in the foothills west of Denver.

Typically, a favorable synoptic environment for a major winter storm along the Front Range of Colorado is achieved only when several factors overlap in space and time. Since the boundary layer along the Front Range is usually very dry, upslope winds are needed to saturate the lower levels of the atmosphere. Air is forced to rise and cool as it moves west across the High Plains of eastern Colorado and eventually up to the Continental Divide. The upslope is usually driven by a cold surface high pressure to the north and/or a lee-side low over southeast Colorado. Moisture aloft is also needed to seed the lower levels: with shallow moisture, the urban corridor experiences freezing drizzle. A cutoff low at 500 mb over the Four Corners region is the ideal location to provide lift in the form of positive vorticity advection and to create an unstable atmosphere due to cold air aloft. The cutoff low typically moves slower, which increases the duration of precipitation.

The two major aspects of this storm that made it a historic event were the depth of the upslope and its duration. The upslope extended from near the surface up to at least 300 mb (Figure 3.1). The fact that there was a closed low at 300 mb over New Mexico suggests that strong easterly winds were present through most of the depth of the troposphere over the Front Range of Colorado. Radar echoes were observed moving west toward the Front Range, another testament of the deep upslope. The extreme snowfall along the Front Range was due to deep upslope (strong forcing) and high moisture content over a long period of time. In Fort Collins, the onset of precipitation occurred during the afternoon of 17 March in the form of rain. Around 0600 UTC on 18 March, the precipitation changed to snow over Fort Collins and remained snow for the duration of the storm. Snowfall was nearly continuous from 0600 UTC on 18 March until it ended around 1800 UTC on 19 March.

3.2 Bright Band Analysis (18 March 2003 at 0600 UTC)

As mentioned earlier, this event started out as all rain. Surface temperatures remained above freezing for several hours after the onset of precipitation, and this situation produced a bright band that was easily observable by the CSU-CHILL radar. Around 0600 UTC on 18 March (11 pm local time, 17 March), a mesoscale phenomena known as a barrier jet (Marwitz and Toth, 1993) rushed south across Fort Collins, and air at the surface at or below freezing was funneled along the foothills. The precipitation quickly changed to snow west of the barrier jet, while precipitation remained liquid east of the boundary as it progressed east away from the foothills. Marwitz and Toth (1993) describe a similar event which occurred on 7 March 1990 with a 500 mb cutoff low of Northern New Mexico in which a barrier jet was observed over southeast Wyoming and northeast Colorado. The barrier jet was found to be a mesoscale front with warmer air and mostly rain to the east and cooler air and snow to the west. Also, evaporation and melting precipitation strengthened the barrier jet. Because of this, the heaviest precipitation fell in the vicinity of this feature as it progressed east from the foothills. This time was chosen for detailed analysis because of the different forms of precipitation observed due to the bright band and barrier jet.

3.2.1 Hydrometeor identification

Hydrometeor identification by means of fuzzy logic was performed on the RHI scan by the CSU-CHILL radar from 18 March 0600 UTC in order to partition the radar image by hydrometeor type so that microphysical quantities could be assigned to each classified hydrometeor. Figure 3.2 shows the observed Z_h, Z_{dr}, and V_r from CHILL at this time. In Figures 3.2-a and 3.2-b, both Z_h and Z_{dr} reach a maximum at around 0.75 km AGL from 5 to 28 km west of the radar. This bright band signature, with snow melting into rain or drizzle as it passes through the 0°C isotherm, is a common radar signature of stratiform rain (Stewart et al., 1984; Fabry and Zawadzki, 1995). What makes this case unique is the overlap in space, about 28 km west of the radar, of the bright band intersecting the ground in Figures 3.2-a and 3.2-b and the wind shift line in Figure 3.2-c. This wind shift is the barrier jet, identified by the wind shifting from easterly east of the boundary to northwesterly west of the boundary. As stated in Marwitz and Toth (1993), the heaviest precipitation is localized in the vicinity of the barrier jet (Figure 3.2a).

The hydrometeor identification result is shown in Figure 3.3. East of 28 km, the frozen to liquid transition in the vertical is spatially consistent with Figures 3.1-a and 3.1-b; however, the transition from snow crystals to liquid should include an intermediate aggregate state because as the snow crystals pass through the -5°C isotherm, they first stick to each other (aggregation) before they completely melt. The breakdown of the fuzzy logic around the bright band is probably due to the sharp changes of Z_h and Z_{dr} over a relatively small distance. At lower levels, two regimes exist: predominantly liquid precipitation east of 28 km from CHILL and predominantly snow aggregates west of 28 km. In the vicinity of the barrier jet (28 km from CHILL), fuzzy logic breaks down again. Since the barrier jet represents the boundary between freezing surface temperatures with snow to the west and warmer surface temperatures with rain to the east, the "rain" around 28 km is probably a rain/snow mix in reality. Since this area contains the highest reflectivites in excess of 40 dBZ (Figure 3.1-a), snow aggregates are not allowed due to the constraints of the mbf's. A rain/snow hydrometeor category would probably take the place of the "rain" around 28 km. With a few exceptions, fuzzy logic performed well (based on physical expectations), and the hydrometeor results agree with theory concerning precipitation type around the bright band and barrier jet.

3.2.2 Microphysical assumptions

Once the hydrometeors are constrained by type, particle densities, shapes, sizes, etc. can be assigned. The quantities arrived at for each particle type were deemed the most appropriate for this storm, as they resulted from an extensive literature search. For example, the range of sizes of snow aggregates found in the literature was narrowed to fit the sizes that were observed during the storm (surface observations taken by author). It is important to realize that the ultimate purpose of this project is to model this storm observed by CHILL at millimeter wavelengths through T-matrix theory. Consequently, hydrometeor identification is primarily used to assign microphysical quantities that are required as inputs for T-matrix. For this time (18 March 0600 UTC) only rain and a rain/snow mix are modeled even though Figure 3.3 also shows snow aggregates and snow crystals present. It is most appropriate to model rain and a rain/snow mix at this transitional time with a bright band and barrier jet. Snow crystals and snow aggregates are best modeled at a later time after the transition where there is no uncertainty in differentiating a rain/snow mix from all snow. It should be mentioned that the model output of the rain/snow category to be discussed in this section does not have unique microphysical assumptions: the microphysical assumptions (T-matrix input) for rain and for snow aggregates are simply modeled simultaneously. Even though the model output of a rain/snow mix (which requires model input from both rain and snow aggregates) will be discussed in this section, the input for snow aggregates will be addressed in the next section, where the model results for snow aggregates are discussed in detail. Also, rain modeled in T-matrix means rain and drizzle in Figure 3.3. Each hydrometeor was averaged over space in order to assign one set of microphysical characteristics per hydrometeor type.

Table 3.1 shows the microphysical assumptions, which are required as input for T-matrix, and the drop size distribution parameters for rain. While N_0 and D_0 are the only inputs into T-matrix concerning the drop size distribution, the mixing ratio and N_t (the total number of hydrometeors per cubic meter) help validate the drop size distribution used and will be discussed shortly. The surface air temperature of 3°C was observed during the storm and is consistent with the presence of raindrops. This temperature is also the reason for some uncertainty in classifying rain/snow vs. snow aggregates mentioned earlier. The T-Matrix model is run once per wavelength, each run consisting of the same microphysical input per hydrometeor. Rain was the easiest hydrometeor to model, because the density of 1 g cm^{-3} is exact. The axis ratio, which is the ratio of the vertical axis and the horizontal axis (assuming the vertical axis is perpendicular to the ground), gives a measure of the prolateness or oblateness of a particle. Since the axis ratio for raindrops changes with size, a formula that takes into account a distribution of axis ratios is required (Jameson, 1983). The elevation angle means the angle of the incident radiation as it encounters the hydrometeor, or simply the elevation angle of the radar. This is important, because the backscattering cross section will change with elevation angle on all particles except homogeneous, perfectly spherical ones. The elevation angle of 2° for rain was obtained by selecting the midpoint of the rain area in Figure 3.3 and calculating the elevation angle as a function of range from the radar. Raindrop sizes typically vary from a minimum of at least 0.2 mm to a maximum of 2 or 3 mm, and the chosen sizes of 1 to 3 mm are appropriate for rain in this storm (Pruppacher and Klett, 1997). The fall mode, or canting angle of hydrometeors can be defined as how much a particle flutters as it is falling, or how much it deviates from falling with its major axis perpendicular to a defined vertical axis. Beard and Jameson (1983) found that canting angles for raindrops (in response to shear in homogeneous, isotropic turbulence) had a standard deviation of at most 4° about a mean of 0°. Hence, a Gaussian distribution was used to model the canting angles, with a mean of 0° and a standard deviation of 4°. The Marshall-Palmer (exponential) drop size distribution from Marshall and Palmer (1948) was used to model rain and is defined as:

$$N(D) = N_0 e^{-\lambda D} \tag{3.1}$$

where N(D) is the number of drops at diameter D, N_0 is the slope intercept, and λ is the slope. Ulbrich (1983) mentions a simple relation for D_0, the mean diameter, and λ:

$$\lambda D_0 = 3.67 \tag{3.2}$$

Because of this relation, λ and D_0 will be used interchangeably throughout the text, even though D_0 is the required input for T-matrix. Marshall and Palmer (1948) define N_0 to be 8×10^4 m^{-3} cm^{-1}. λ was calculated through the Z-R relationship $Z= 200R^{1.6}$ (Battan, 1973). The mixing ratio and N_t are calculated from the drop size distribution parameters in order to verify that the Z-R relationship and drop size distribution parameters are accurate representations. Both a mixing ratio of 0.33 g kg^{-1} (Rutledge and Hobbs, 1983) and the calculated N_t are reasonable for rain; therefore, the drop size distribution used appears to fit the storm well.

3.2.3 T-matrix output

Table 3.2 shows the model results for rain. All of the values for S-band are within the expected ranges (Lhermitte, 1990). Moving from S-band down to Ku, Ka, and W-band means that at each successive wavelength, more of the rain medium is in the Mie regime. In Mie scattering, there is enhanced forward scattering, reducing the backscattered radiation. This reduction of backscattering cross section is evident in the reduction of Z_h at W-band. However, because of the oscillatory nature of the Mie regime, Z_h is actually higher at Ku-band than at S-band for the specific sizes chosen. The oscillatory nature of the Mie regime is illustrated in Figure 3.4 (Lhermitte, 1990). At 35 GHz (Ka-band), raindrops around 2 mm actually have a larger backscattering cross section with Mie scattering compared to Rayleigh. At 94 GHz (W-band), the backscattering cross section is severely diminished with Mie scattering. The Z_{dr} values are slightly positive, which describe an oblate spheroid like a raindrop. Positive K_{dp} values indicate that there is more phase shift in the horizontal than in the vertical, which is the case for oblate particles like raindrops. The 0 Z_{dr} and negative K_{dp} at W-band are due to strong Mie scattering effects. Attenuation increases as wavelength decreases because of the increase in the scattering cross section (Q_s).

In an attempt to model a rain/snow mix, the input for rain and the input for snow aggregates (to be discussed in the next section) were modeled together. The model output for a rain/snow mix is very similar to the model output for rain alone, as expected (Table 3.3). Since the density of rain is at least an order of magnitude larger than that of snow aggregates, given a unit volume of air with rain and snow, the radar will see the rain as dominant, because it has the larger dielectric response. The modeled Z_h at S-band, 35 dBZ, is lower than what was observed as a rain/snow mix around 28 km in Figure 3.2-a. This is probably due to the fact that in the calculation of λ in the drop size distribution for rain, an average value of the observed reflectivity was used. In the vicinity of the barrier jet, the rain and/or snow was locally heavy. Because of the uncertainty of hydrometeor type in this vicinity, the input for modeling rain was used even though the observed reflectivity was averaged.

3.3 Analysis on 19 March 2003 at 0000 UTC

Approximately 18 hours after the bright band case, the precipitation had become more uniform. All of the precipitation was snow, as the northerly surge behind the barrier jet had encompassed the entire urban corridor. As far as rate of accumulation of snowfall in the Fort Collins area, the storm was at its peak. The observations tally a little more than a foot of snow on the ground at this time, and approximately another foot and half fell for the next 18 hours until the precipitation finally ended. This time was chosen because it typified the storm as a whole, both with respect to precipitation coverage and intensity.

3.3.1 Hydrometeor identification

The same reasoning and assumptions hold for this time as for the previous one. For example, Z_h, Z_{dr}, and temperature were used in fuzzy logic for hydrometeor classification. Also, the same mbf's were used. Figure 3.5 shows the observed Z_h, Z_{dr}, and V_r from CHILL. One drastic difference when this time is compared with the previous (Figures 3.2a-c) is that the Z_h, Z_{dr}, and V_r plots are more layered (Figures 3.5a-c). Looking at Figure 3.5a, there is more uniform and widespread coverage of the precipitation. Notice that reflectivities of greater than 25 dBZ are widespread, meaning that heavy snow is present over the Fort Collins vicinity. The Z_{dr} values range from 1 dB to between –1 and 0 dB (Figure 3.5b). The largest vertical gradient in Z_{dr} is located at about 2 km AGL, with higher values above this level and lower values below this level. This means that dendritic snow crystals are aggregating into snowflakes at about 2 km AGL. In Figure 3.5c, the northerly surge at the surface has encompassed the entire range of the radar, turning all of the precipitation to snow. The upslope is also shown to be incredibly deep, as mentioned before. Strong upslope up to 15 m/s is observed up to 5 km AGL.

The hydrometeor identification results are shown in Figure 3.6. Ignoring the three points misclassified as rain, all of the precipitation is snow. Also, the snow crystal/snow aggregate line of demarcation is right at 2 km AGL. This agrees with the hypothesis made regarding the level of aggregation based on Figure 3.5b. Unlike the hydrometer identification results for 0600 UTC on 18 March 2003, there is no uncertainty with respect to the hydrometeor classification. The snow was well observed at this time, and the results are simple to interpret.

3.3.2 Microphysical assumptions

Snow is more difficult to model than rain, due to uncertainties about shape and density. The degree of riming also introduces uncertainties. For these reasons, both snow crystals and snow aggregates were modeled at various densities. The first run used densities of 0.09 g cm^{-3} for snow aggregates and 0.45 g cm^{-3} for snow crystals that were derived from an extensive literature search. The second run held everything else constant and used densities of 0.02 g cm^{-3} for snow aggregates and 0.1 g cm^{-3} for snow crystals (Dr. Andy Heymsfield, NCAR, personal communication). Since the second density used was lower than what the literature suggested in both cases, the modeled Z_h was substantially reduced. This is due to the fact that the particle size distributions used in both runs assumed the higher density found in the literature. For this reason, adjustments were made to the particle size distribution parameters until the Z_h for the runs with the lower density matched the Z_h output from the runs with the higher, literature-based density. Therefore, there are a total of 12 runs for each hydrometeor type (crystals and aggregates), that breakdown as one run per wavelength for the original density plus one run per wavelength for the new, lower density plus one run per wavelength for the new, lower density with the adjusted particle size distribution parameters. These adjustments will be explained shortly.

The model input for snow aggregates is shown in Table 3.4. A surface air temperature of -3° C was observed at this time, and was used as model input. Just as before, all hydrometeors are modeled at S-band, Ku-band, Ka-band, and W-band. A bulk density of 0.09 g cm^{-3} was taken from the literature and was the density assumed in the particle size distribution used (Pruppacher and Klett, 1997; Passarelli, 1978). As mentioned before, a bulk density of 0.02 g cm^{-3} was used in the second run. An axis ratio of 0.8 was used, meaning that the snow aggregates were oblate (Barthazy and Schefold, 2003). An elevation angle of 2° was assumed. Sizes of snow aggregates can range from one or several millimeters to several centimeters (Pruppacher and Klett, 1997). Based on observations, sizes from 1 mm to 1.5 cm were chosen. A canting angle with a Gaussian distribution, a mean of 0°, and a standard deviation of 30° was used allowing the snowflakes to wobble with respect to their orientation with the ground as they fall. The particle size distribution used was the Marshall-Palmer distribution (Marshall and Palmer, 1948), and the parameters are defined exactly the way they were previously. Passarelli (1978) used in-situ data to collect distributions of snow aggregates and then calculated the slope and intercept parameters of the distributions. An N_0 of 5.1 X 10^5 m^{-3} cm^{-1} and slope (λ) of 24.4 cm^{-1} were used and the density assumed was 0.09 g cm^{-3}. The mixing ratio of 0.41 g cm^{-3} agrees well with the values from Rutledge and Hobbs (1983). Keeping everything else constant, notice the decline in the mixing ratio to 0.1 g cm^{-3} when a density of 0.02 g cm^{-3} is used (Table 3.4). In order to achieve physically acceptable reflectivities with less total mass (discussed earlier), the intercept and slope parameters had to be adjusted in such a way as to conserve the total mass of 0.1 g kg^{-1} while increasing Z_h. The only way to do this is to change the distribution by allowing more larger snow aggregates by decreasing the slope and decreasing the intercept until the resultant Z_h matches the output from the run with a density of 0.09 g cm^{-3}. Using this guess and check method, a new N_0 of 9.5 X 10^3 m^{-3} cm^{-1} and a new λ of 9 cm^{-1} were arrived at. Notice that the total mass is the same and the total number per cubic meter has gone down, but a greater proportion of these particles are larger ones.

Table 3.5 shows the model input for snow crystals (a dendritic type was assumed). An air temperature of -15°C was derived from the Eta model sounding and was used. Snow crystals are also modeled over all four wavelengths. A bulk density of 0.45 g cm^{-3} was found in the literature and was used in the first run (Heymsfield, 1972), and a bulk density of 0.1 g cm^{-3} was used in the second run (discussed earlier). The axis ratio of 0.15 is a testament of flat, dendritic crystals, and was calculated from an empirical formula in Heymsfield (1972). An elevation angle of 5° was assumed. The diameters of the dendritic crystals modeled were from 0.5 mm to 3.5 mm (Pruppacher and Klett, 1997). No canting was assumed in modeling crystals, meaning that it was assumed the dendrites fell with their major axis parallel to the ground (Bringi and Chandrasekar, 2001). The drop size distribution used was Marshall and Palmer (1948). The slope (λ) and intercept (N_0) parameters were calculated from in-situ data from several data sets (Heymsfield et al., 2002). Again, in order to account for the lower total mass when the lower density is used, λ and N_0 must be adjusted in such a way that mass is conserved, but Z_h values are reasonable in the output. Through a guess and check process, a new N_0 of 4.35×10^3 m^{-3} cm^{-1} and a new lambda of 12 cm^{-1} were calculated.

3.3.3 T-matrix output

Table 3.6 contains the model output for snow aggregates. The quantities calculated for S-band using a density of 0.09 g cm^{-3} are very reasonable (Lhermitte, 2002). The Z_h is very typical of moderate snow, and the near 0 dB value for Z_{dr} is indicative of the approximately spherical snow aggregates. Since the snow aggregates are approximately spherical, there is little difference between phase shifts in the horizontal and vertical, resulting in a low value for K_{dp}. The output for ρ_{hv} at S-band is typical, and attenuation is very low, as expected, because snow is a much weaker dielectric than rain. Comparing this run to S-band with a density of 0.02 g cm^{-3} and the same N_0 and λ, the reflectivity drops considerably, a result of decreasing the total mass. Even though the original reflectivity of 21 dBZ is recovered in the third run for S-band by changing N_0 and λ as discussed earlier, the LDR is much lower with both of the runs using the density of 0.02 g cm^{-3} when compared to the first run. Since LDR is the ratio of the cross-polar signal to the co-polar signal and is low to begin with, making the snowflakes even less dense (there is literally less dielectric to interact with the radar wave) would make the cross-polar signal less discernable, leading to a low LDR. The exception is W-band, where LDR actually increases in the last run with lower density. This is due to strong Mie scattering effects. The same basic patterns hold for the other wavelengths when observing how Z_h and LDR change with different density. The other quantities in Table 3.6 (Z_{dr}, K_{dp}, ρ_{hv}, and attenuation) are not affected by changing the density.

Now, comparing the different wavelengths over the same density, N_0, and λ, predictable patterns are apparent. Looking at S-band through W-band at a density of 0.09 g cm^{-3}, Z_h decreases as the wavelength decreases. This is due to an average increase of forward scattering as the wavelength is decreased because of stronger Mie scattering. Regarding the difference in Z_h between centimeter and millimeter wavelength radars due to the transition from Rayleigh to Mie scattering, Matrosov (1998) measures similar values. There is little change in Z_{dr} as wavelength is varied. The drastic increase in LDR with W-band is again the result of Mie scattering, specifically the oscillatory backscattering behavior. K_{dp} increases with decreasing wavelength; according to Bringi and Chandrasekar (2001), this behavior is shown to be valid down to 35 GHz (Ka-band). The output values of K_{dp} in Table 3.6 also increase at W-band. Since this behavior has no theoretical basis at 95 GHz, the large K_{dp}'s at this wavelength must me attributed to strong Mie effects or other factors. ρ_{hv} seems to not be affected as much with wavelength. Attenuation drastically increases as wavelength decreases, because in the Mie regime more of the incident radiation is being scattered away in all directions along the path of the radar beam. These same patterns also hold when the other sets of runs, one for a density of 0.02 g cm^{-3} with the same N_0 and λ and the other for a density of 0.02 g cm^{-3} with a different N_0 and λ, are examined. In general, the undeterminable (high LDR's, for example) polarimetric quantities in all three W-band runs can be attributed to increased forward scattering and oscillatory back scattering cross sections in the Mie regime, and the fact that scattering and attenuation by snowflakes in the Mie regime has no theoretical basis because of their complex shape (Lhermitte, 2002).

Similar to the snow aggregates, decreasing the density of the snow crystals causes significant changes in some of the model-derived radar quantities (Table 3.7). Z_h and Z_{dr} are significantly reduced when S-band at a density of 0.45 g cm^{-3} is compared with S-band at a density of 0.1 g cm^{-3} with the same N_0 and λ. Since a dendritic snow crystal has the shape of a pancake, its Z_{dr} should be large and positive. The low LDR and small K_{dp} correspond with the unrealistic Z_{dr} value at S-band. Also, since the original reflectivity of 17.4 dBZ could not fully be recovered using a density of 0.1 g cm^{-3} and by altering N_0 and λ (the third run for S-band), the values mentioned above for the polarimetric quantities may reflect a physically unlikely particle size distribution. This is evident in Table 3.5, where N_t in this hypothetical particle size distribution is only 363 particles m^{-3}. The changes in the model output from one density to the other for the other frequencies are similar. Any further analysis on the runs with the lower density could be futile, due to the fact that the model values may be the result of an unphysical particle size distribution. It could be that 0.01 g cm^{-3} is too low of a density for the particle size distribution used.

Concentrating on the first set of runs in Table 3.7 with the density at 0.45 g cm^{-3}, reflectivity decreases as wavelength decreases as expected. Just like with snow aggregates, forward scattering is enhanced for Mie scatterers. The Z_{dr} at each wavelength is highly positive, as would be expected from an oblate-shaped hydrometeor. The higher values of K_{dp} with dendritic snow crystals (when compared to snow aggregates) are due to their shape: they are more oblate and cause a larger phase shift in the horizontal than in the vertical. The K_{dp} values increase with decreasing wavelength. This behavior is validated in Bringi and Chandrasekar (2001) only down to Ka-band; the behavior at W-band is unpredictable and must be attributed to strong Mie scattering. The attenuation dramatically increases as wavelength decreases for the same reason mentioned in the snow aggregate analysis.

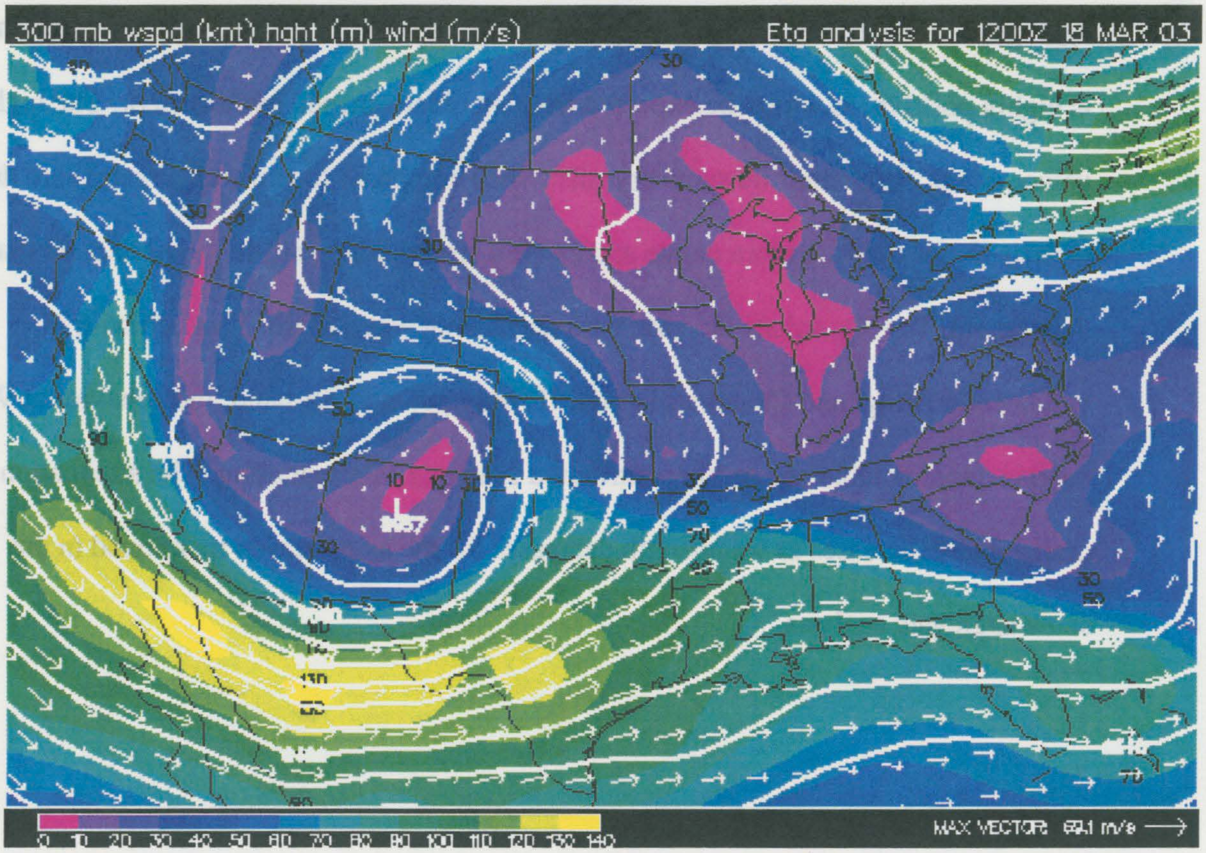

Figure 3.1: 300 mb analysis for 1200 UTC on 18 March 2003 from Unisys Weather. (URL: http://weather.unisys.com/archive/eta_init/0303/03031812.gif, 2003)

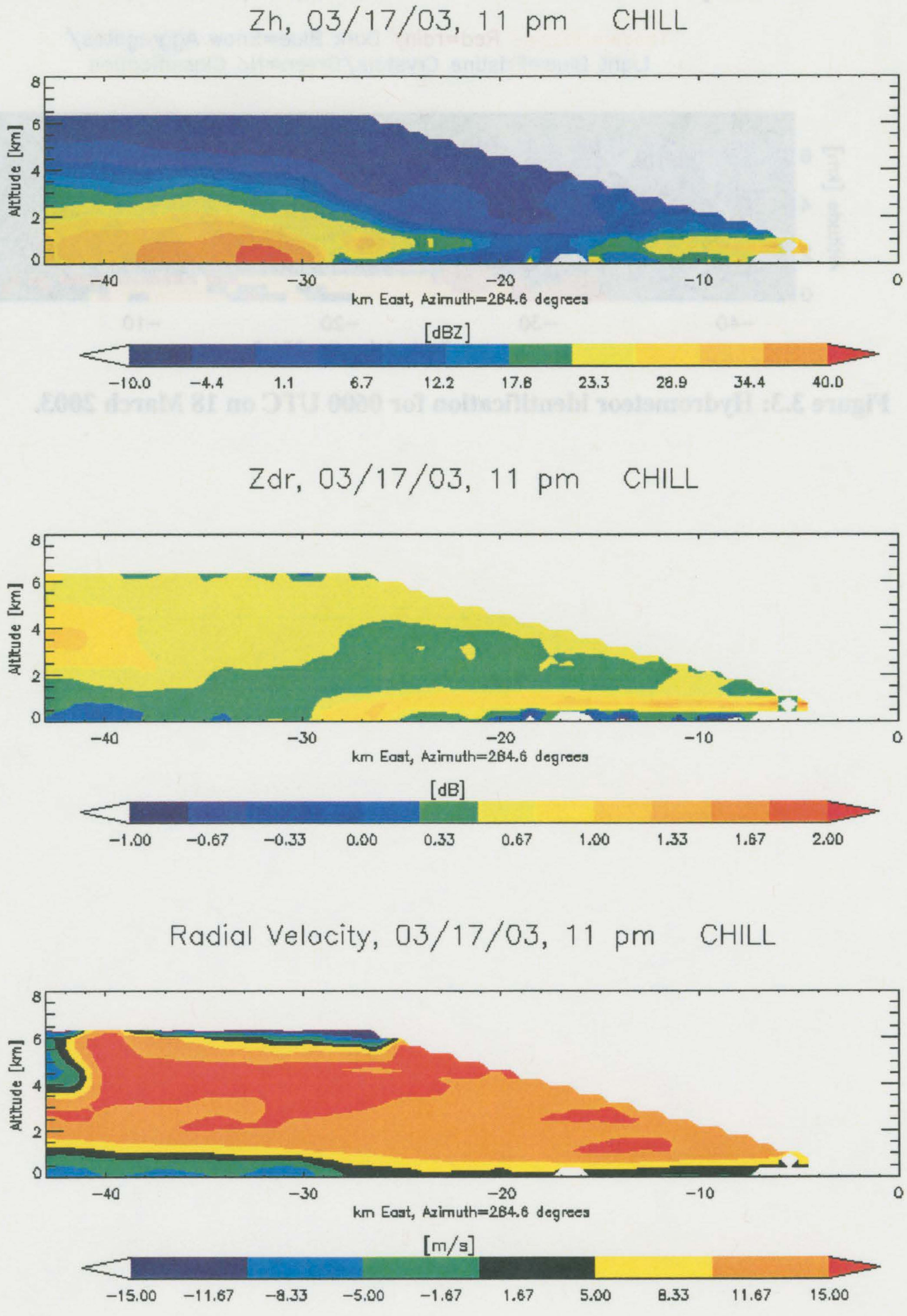

Figure 3.2: CHILL RHI scan for 0600 UTC on 18 March 2003 of (a) Z_h, (b) Z_{dr} and (c) radial velocity.

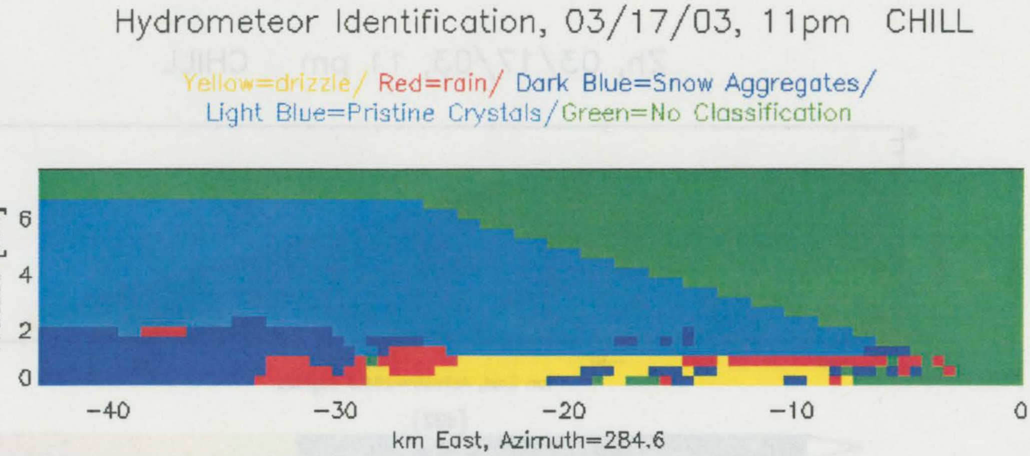

Figure 3.3: Hydrometeor identification for 0600 UTC on 18 March 2003.

Table 3.1: Microphysical assumptions for rain.

Model Input Rain (11pm MST, March 17th, 2003)

T-Matrix				*Mueller*		
Air Temp. [° C]	Radar Wavelength [cm]	Bulk Density [g cm^{-3}]	Axis Ratio	Elevation Angle [degrees]	Particle Diameter [cm]	Fall Mode (Gaussian) [degrees]
3.0	11.0 (S-band)	1.0	Factor Of Size	2.0	0.1-0.3 (Step: .05)	Mean: 0.0 Standard Deviation: 4.0
	2.2 (Ku-band)					
	0.84 (Ka-band)					
	0.32 (W-band)					

Drop Size Distribution Parameters for Rain

Bulk Density [g cm^{-3}]	λ [cm^{-1}] / D_0 [cm]	N_0 [cm^{-1} m^{-3}]	Mixing Ratio [g m^{-3}]	N_t [# m^{-3}]
1.0	28.2 / 0.13	80,000	0.33	2,837

Table 3.2: T-matrix output for rain.

Model Output for Rain (11pm MST, March 17th, 2003)

Run Description	Z_h [dBZ]	Z_{dr} [dB]	LDR [dB]	K_{dp} [deg. km^{-1}]	ρ_{hv}	Specific Horizontal Attenuation [dB km^{-1}]
S-band	35.0	0.21	-37.5	0.02	0.9998	0.002
Ku-band	35.1	0.25	-35.9	0.12	0.9998	0.17
Ka-band	34.8	0.18	-36.2	0.18	0.9998	1.46
W-band	17.7	0.0	-41.0	-0.17	0.9999	3.39

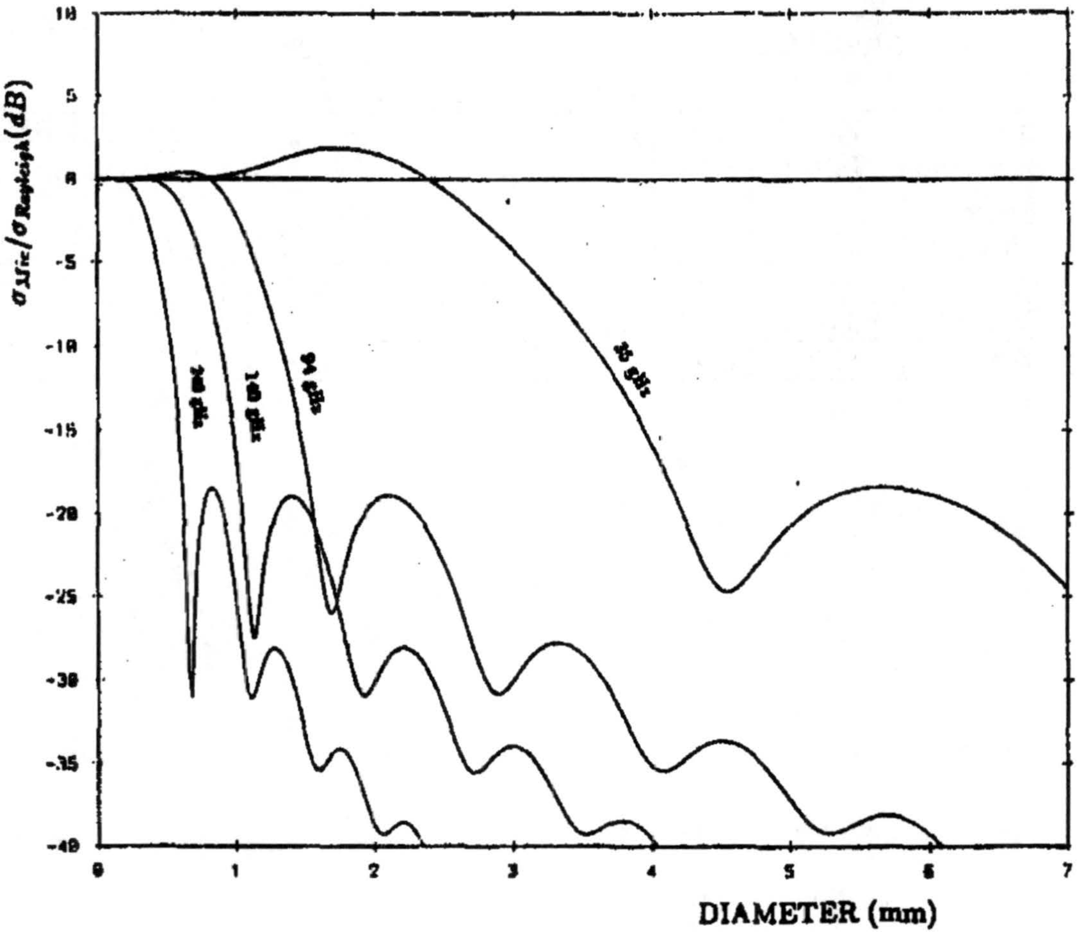

Figure 3.4: Ratio of Mie to Rayleigh backscattering cross sections at various radar frequencies (35 GHz, 94 GHz, 140 GHz, and 240 GHz) and particle diameters (Lhermitte, 1990).

Table 3.3: T-matrix output for rain and snow aggregates.

Model Output for Rain/Aggregates [ρ(ice)=0.09 g cm^{-3}]
(11pm MST, March 17th, 2003)

Run Description	Z_h [dBZ]	Z_{dr} [dB]	LDR [dB]	K_{dp} [deg. km^{-1}]	ρ_{hv}	Specific Horizontal Attenuation [dB km^{-1}]
S-band	35.0	0.21	-37.6	0.03	0.9998	0.002
Ku-band	35.2	0.25	-36.0	0.14	0.9998	0.17
Ka-band	35.0	0.18	-36.3	0.24	0.9998	1.48
W-band	17.8	0.0	-38.7	-0.02	0.9997	3.62

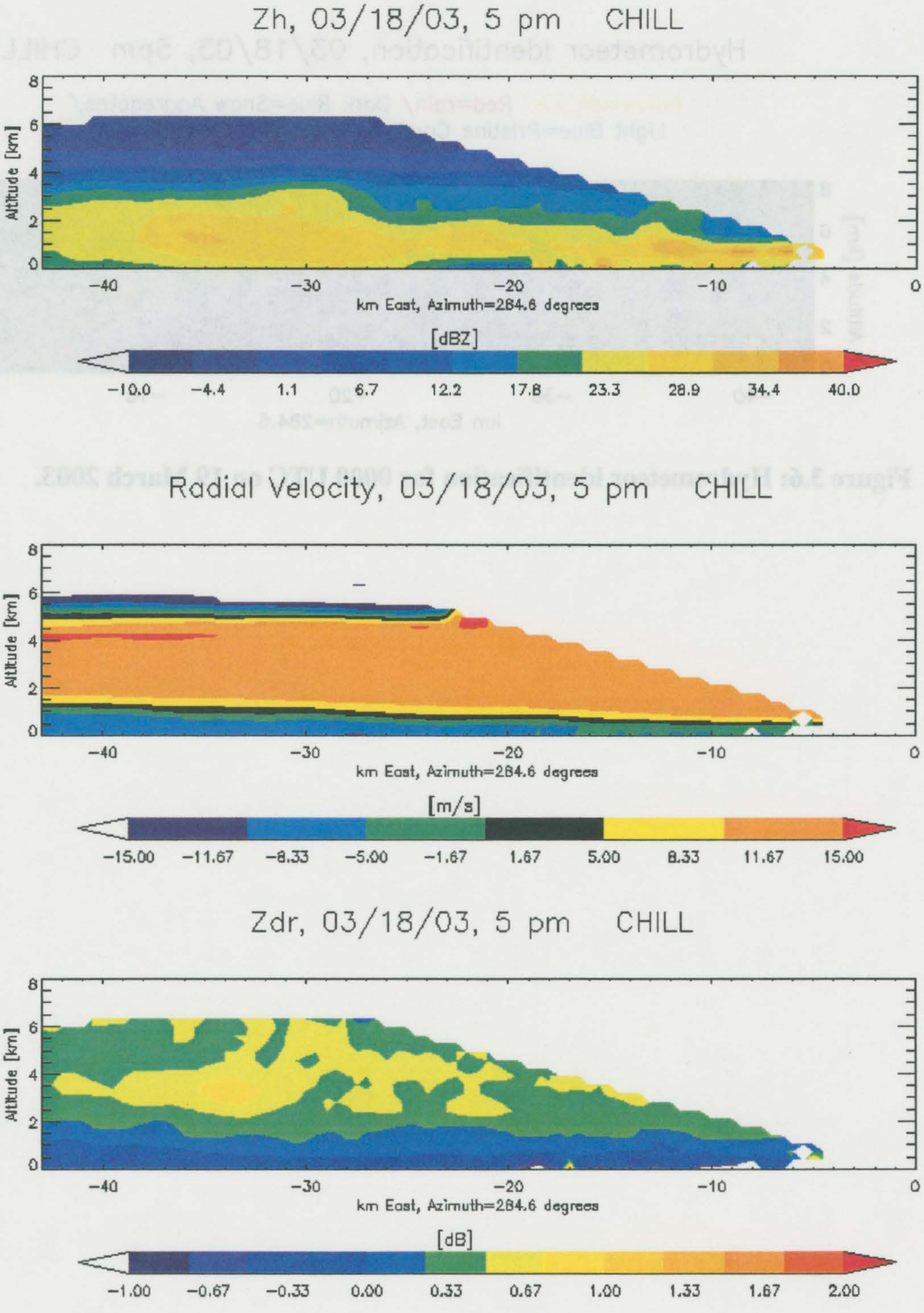
Zh, 03/18/03, 5 pm CHILL

Radial Velocity, 03/18/03, 5 pm CHILL

Zdr, 03/18/03, 5 pm CHILL

Figure 3.5: CHILL RHI scan for 0000 UTC on 19 March 2003 of (a) Z_h, (b) Z_{dr} and (c) radial velocity.

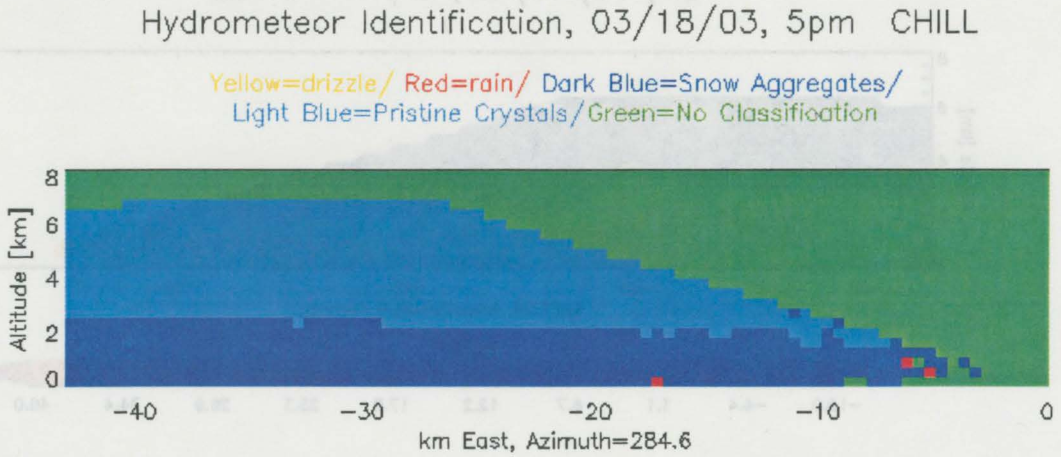

Figure 3.6: Hydrometeor identification for 0000 UTC on 19 March 2003.

Table 3.4: Microphysical assumptions for snow aggregates.

Model Input for Snow Aggregates (5pm MST, March 18th, 2003)

T-Matrix				*Mueller*		
Air Temp. [° C]	Radar Wavelength [cm]	Bulk Density [g cm^{-3}]	Axis Ratio	Elevation Angle [degrees]	Diameter [cm]	Fall Mode (Gaussian) [degrees]
-3.0	11.0 (S-band)	**0.09**	0.8	2.0	0.1-1.5 (Step: 0.1)	Mean: 0.0 Standard Deviation: 30
	2.2 (Ku-band)					
	0.84 (Ka-band)					
	0.32 (W-band)					
-3.0	11.0 (S-band)	**0.02**	0.8	2.0	0.1-1.5 (Step: 0.1)	Mean: 0.0 Standard: Deviation: 30
	2.2 (Ku-band)					
	0.84 (Ka-band)					
	0.32 (W-band)					

Particle Size Distribution Parameters for Snow Aggregates

Bulk Density [g cm^{-3}]	λ [cm^{-1}] / D_0 [cm]	N_0 [cm^{-1} m^{-3}]	Mixing Ratio [g m^{-3}]	N_t [# m^{-3}]
0.09	24.4 / 0.15	**510,000**	0.41	20,902
0.02	24.4 / 0.15	**510,000**	0.1	20,902
	9.0 / 0.41	**9,513.45**	0.1	1,057

Table 3.5: Microphysical assumptions for dendritic snow crystals.

Model Input for Snow Crystals [dendrites] (5pm MST, March 18th, 2003)

T-Matrix				*Mueller*		
Air Temp. [° C]	Radar Wavelength [cm]	Bulk Density [g cm^{-3}]	Axis Ratio	Elevation Angle [degrees]	Diameter [cm]	Fall Mode (Gaussian) [degrees]
-15.0	11.0 (S-band)	**0.45**	0.15	5.0	0.05-0.35 (Step: 0.1)	Mean: 0.0 Standard Deviation: 0.5
	2.2 (Ku-band)					
	0.84 (Ka-band)					
	0.32 (W-band)					
-15.0	11.0 (S-band)	**0.10**	0.15	5.0	0.05-0.35 (Step: 0.1)	Mean: 0.0 Standard: Deviation: 0.5
	2.2 (Ku-band)					
	0.84 (Ka-band)					
	0.32 (W-band)					

Particle Size Distribution Parameters for Snow Crystals

Bulk Density [g cm^{-3}]	λ [cm^{-1}] / D_0 [cm]	N_0 [cm^{-1} m^{-3}]	Mixing Ratio [g m^{-3}]	N_t [# m^{-3}]
0.45	50.0 / 0.07	**1,333,521**	0.041	26,670
0.10	50.0 / 0.07	**1,333,521**	0.01	26,670
	12.0 / 0.31	**4,355**	0.01	363.0

Table 3.6: T-matrix output for snow aggregates. ρ(ice), the bulk density, and N_0 are in the same units as Table 3.4.

Model Output for Snow Aggregates (5pm MST, March 18th, 2003)

Run Description	Z_h [dBZ]	Z_{dr} [dB]	LDR [dB]	K_{dp} [deg. km^{-1}]	ρ_{hv}	Specific Horizontal Attenuation [dB km^{-1}]
S-band / **ρ(ice)=0.09** **N_0=510,000**	21.1	0.05	-49.7	0.004	0.9999	0.00007
Ku-band / same	20.5	0.06	-49.4	0.02	0.9999	0.0005
Ka-band / same	17.1	0.07	-47.9	0.06	0.9999	0.01
W-band / same	2.1	0.09	-26.5	0.2	0.9945	0.2
S-band / **ρ(ice)=0.02** **N_0=510,000**	8.0	0.01	-62.8	0.0002	0.9999	0.00002
Ku-band / same	7.4	0.01	-62.5	0.001	0.9999	0.00005
Ka-band / same	4.0	0.01	-61.0	0.003	0.9999	0.0007
W-band / same	-11.0	0.02	-27.2	0.006	0.9953	0.01
S-band / **ρ(ice)=0.02** **N_0=9,513.45**	21.0	0.01	-62.7	0.0003	0.9999	0.00002
Ku-band / same	17.0	0.01	-61.0	0.001	0.9999	0.0003
Ka-band / same	5.2	0.02	-31.0	0.003	0.9980	0.005
W-band / same	-9.2	0.6	-3.84	-0.05	0.4310	0.04

Table 3.7: T-matrix output for dendritic snow crystals. ρ(ice), the bulk density, and N_0 are in the same units as Table 3.5.

Model Output for Snow Crystals [dendrites] (5pm MST, March 18th, 2003)

Run Description	Z_h [dBZ]	Z_{dr} [dB]	LDR [dB]	K_{dp} [deg. km^{-1}]	ρ_{hv}	Specific Horizontal Attenuation [dB km^{-1}]
S-band / **ρ(ice)=0.45** **N_0=1333521**	17.4	3.5	-52.3	0.13	0.9999	0.000018
Ku-band / same	16.9	3.6	-52.2	0.66	0.9999	0.0002
Ka-band / same	13.7	3.8	-51.8	1.8	0.9999	0.007
W-band / same	4.0	4.1	-51.0	5.2	0.9953	0.18
S-band / **ρ(ice)=0.10** **N_0=1333521**	3.3	0.8	-63.7	0.007	0.9999	0.000003
Ku-band / same	2.7	0.8	-63.6	0.04	0.9999	0.00001
Ka-band / same	-0.7	0.86	-63.5	0.09	0.9999	0.0003
W-band / same	-11.2	0.87	-62.2	0.25	0.9987	0.005
S-band / **ρ(ice)=0.10** **N_0=4,355**	14.6	0.82	-63.7	0.0086	0.9999	0.000004
Ku-band / same	12.5	0.84	-63.4	0.04	0.9999	0.00009
Ka-band / same	2.0	0.91	-62.7	0.12	0.9870	0.002
W-band / same	-9.0	2.8	-40.2	0.27	0.2203	0.03

Chapter 4

THE OCTOBER 1997 BLIZZARD

4.1 Storm Overview and Synoptic Environment

The October 1997 storm was a true blizzard as defined by the National Weather Service. Less total snow fell along the Front Range when compared to the March 2003 snowstorm, but colder temperatures and stronger winds characterized this storm. A total of 19 inches (41.8 cm) of snow fell on Fort Collins. Unlike the March 2003 snowstorm, deep snow fell on the eastern plains of Colorado due to the colder air. Blizzard conditions buried Interstate 25, and cars were left abandoned along the Front Range.

The basic synoptic pattern discussed earlier was observed during this storm, as all major Front Range winter storms need the same key factors to come together. However, there were some important differences that made this storm colder and stronger, despite its faster movement. The high pressure center over Wyoming characterized a colder air mass, which created a stronger surface pressure gradient over eastern Colorado. The cutoff low at 500 mb was located directly over the Four Corners region instead of in northern New Mexico like the March 2003 storm. The atmosphere was more unstable, because the colder air under the 500 mb low was directly over Colorado. This suggests that there was imbedded convection and heavier, more intense snowfall. Notice the very cold cloud tops over the Front Range, in this case indicative of intense precipitation (Figure 4.1). The duration of precipitation at Fort Collins with this storm was about 24 hours, from roughly sunrise on 24 October to sunrise on 25 October. Overall, the October 1997 blizzard was a more intense storm in terms of dynamics (positive vorticity advection and wind speed) when compared to the March 2003 storm, which had deeper upslope and lasted much longer.

4.2 Data Methods and Analysis

The second half of this thesis focuses on graphical output from the T-matrix model instead of the tabular output contained in the last chapter, as radar images were made from several hundred grid points of output from the T-matrix model (in combination with a cloud model) for most of the situations examined. In this way we could see how millimeter wavelength radars perform in observing a snowstorm when compared to S-band radars. The purpose, as stated in the introduction, is to see if on one hand, the millimeter wavelength radars offer an economical or scientific advantage over S-band radars and on the other hand, if attenuation and Mie scattering effects render the millimeter radars ineffective at times. To insure that the modeled radar image resembled reality, the modeled S-band wavelength radar images were compared to the CSU-CHILL observed radar images at the same orientation and time. Also, to insure that the modeled wavelength radars looked like radar images, over 400 grid points defined the grid for each radar image. This degree of detail demands different input values at each grid point, unlike the method of spatially-averaging each hydrometeor type employed in the last chapter. This input comes from the Regional Atmospheric Modeling System (RAMS) model, a microphysical model developed in the Colorado State University's Department of Atmospheric Science (Meyers, et al., 1997; Walko, et al., 1995). While the previous approach generated T-matrix model output values from a user-defined hydrometeor sample, the approach in this chapter applies the T-matrix method to RAMS model outputs.

4.2.1 Microphysical assumptions

The T-matrix model is actually two sets of codes, T-matrix and Mueller, as stated in Chapter 2. Since the T-matrix code actually calculates the scattering of one particle in a laboratory setting and the particle size distribution and radar inputs are not implemented until the Mueller code, the T-matrix code input can actually be prescribed for each specific hydrometeor as to not change over the 400 plus grid points in the radar image. In other words, one set of prescribed inputs is needed for each hydrometeor that is modeled on the grid. This prescribed input per hydrometeor is the air temperature, radar wavelength, bulk density, and axis ratio. In modeling the RAMS data, it was assumed that these properties plus the fall mode did not change from grid point to grid point for a specific hydrometeor. The elevation angle, diameters, and particle size distribution were all allowed to change from grid point to grid point for each hydrometeor species present.

The RAMS model is a high-resolution microphysical model that was selected to provide most of the microphysical input to the T-matrix model. The model was initialized at 0000 UTC on October 25, 1997 and was allowed to "spin up" for 3 hours. At 0300 UTC, the modeled microphysics were extracted as gridded data sets. This time was selected, because the precipitation was well developed over the Fort Collins area. A vertical cross section that started east of Interstate 25, went through Fort Collins, and ended at the base of the foothills was selected from the larger, three dimensional grid. The vertical cross section was 45 km east to west and extended from the surface to 8 km AGL. These dimensions contained a grid that was 16 grid points from east to west and 26 grid points in the vertical, a total of 416 grid points. Contained in each of these grid points in the form of a data file for each hydrometeor were the mixing ratio expressed in g kg^{-1}, and the total number concentration expressed in # kg^{-1} and # m^{-3}. From these three quantities, all of the microphysical values from RAMS could be calculated. The only hydrometeors that RAMS generated for this time and cross section chosen were snow aggregates and dendritic snow crystals. The Mueller code was looped over each grid point taking input per hydrometeor from both the unchanging T-matrix input quantities and the changing RAMS data set. The Mueller program calculated radar output for each hydrometeor, and then combined them to get a total Z_h, Z_{dr}, LDR, K_{dp}, ρ_{hv}, and attenuation for each grid point.

For the snow aggregates, a temperature of -5°C (23° F) is typical for this type of storm and was chosen. The same radar wavelengths were used, S, Ku, Ka, and W-band, and the grid had to be modeled for each wavelength. A density of 0.1 g cm^{-3} was calculated from empirical mass-size relationships that RAMS uses (Locatelli and Hobbs, 1974). An axis ratio of 0.8 was again used to model snow aggregates (Barthazy and Schefold, 2003). These four microphysical quantities were input into the T-matrix code, and the output was saved so that when the Mueller code was looped over the entire grid with its changing inputs for snow aggregates (particle size distribution, for example), the

T-matrix output served as a fixed input. The elevation angle was calculated per grid point as the Muller program was looped over the grid (method discussed shortly). The diameter range and step were defined and fixed before looping over the grid; however, the sizes were allowed to vary with each grid point. Snow aggregate diameters were allowed to vary from 0.1 mm to 1 cm at a step of 0.1 mm. This range and step was extracted from the RAMS code prior to running the model. The canting angle was fixed as it was in the previous chapter as a Gaussian distribution with a mean of 0° and a standard deviation of 30°. A different particle size distribution was calculated for each grid point, depending on the mixing ratio and N_t for snow aggregates modeled by RAMS. Instead of using an exponential distribution, a gamma distribution was used of the form (Ulbrich, 1983):

$$N(D)=N_0D^{\mu}e^{-\lambda D} \tag{4.1}$$

All of the parameters are the same as the exponential distribution, with the added factor of D^{μ}. The dispersion factor, μ, affects the shape of the distribution. This distribution looks just like the exponential distribution when plotted, except that it has a tail toward the smaller sizes (which depends on μ) instead of being linear with an intercept. The shape of the distribution can be changed or shifted, allowing different numbers of different sizes, by changing μ. An example of a gamma distribution can be seen in Figure 4.2; this distribution of snow aggregates was calculated by RAMS and was one of several hundred used as input for the T-matrix model. An exponential distribution has a μ of 0, reducing Eq. 4.1 to Eq. 3.1. Therefore, the T-matrix model (Mueller code) needs N_0, λ, and μ as inputs for the particle size distribution. The RAMS model had a fixed μ of 1 while generating the data files, so μ was simply fixed as input. Care needed to be taken while calculating N_0 and λ, because the gamma distribution is in a different form in the

RAMS model (Meyers, et al., 1997). λ was calculated from the mixing ratio and N_t, which were both read off of the RAMS data file. N_0 was calculated from the parameters ν and N_t. The parameter ν is the dispersion factor in the RAMS version of the gamma distribution. This changing particle size distribution is what really determines the diameters of the snow aggregates at each grid point. By specifying λ, N_0, and μ at each grid point, the particle size distribution is determined. From this, the number of particles at each size is constrained.

The inputs for dendritic snow crystals followed the same methods as those for the snow aggregates. A temperature of –15°C used in the last chapter was also used in this case. Again, the model has to be run once per wavelength. A bulk density of 0.25 g cm^{-3} was calculated as it was for snow aggregates, using a mass-size relationship from the RAMS code (Locatelli and Hobbs, 1974). An axis ratio of 0.04 was calculated, defining a dendrite snow crystal (Heymsfield, 1972). These inputs represent the T-matrix code inputs that will be held constant for snow crystals throughout the grid. Since snow crystals and snow aggregates occupy the same grid point when they coexist, the elevation angle would be the same for both hydrometeors for the same grid point, and the calculation will be discussed shortly. The diameters are allowed to vary from grid point to grid point, because they are constrained by the particle size distribution. However, a fixed range of 0.1 mm to 1 cm with a fixed step of 0.1 mm was extracted from the RAMS code. The fall mode used is the same as it was in the previous chapter, allowing no canting (Bringi and Chandrasekar, 2001). The particle size distribution parameters, N_0, μ, and λ, were calculated in the same way as with the snow aggregates. Each grid point, assuming that RAMS modeled snow crystals in that grid point, contained a data file that contained the mixing ratio and N_t. These were then used to calculate N_0 and λ.

4.2.2 Calculations on the grid

Considerable programming was needed to do some of the calculations to change an arbitrary grid of data into a radar image. Since this grid was a vertical slice, it could be transformed into an RHI image commonly observed by radars such as CHILL. The radar was "placed" on the eastern end of the grid at ground level in order to mimic a CHILL RHI over the Fort Collins vicinity. All of the calculations discussed depend on the location of the radar (viewing geometry).

The elevation angle that is needed as input into the T-matrix model changes at each grid point. To calculate this, the radar was assigned at a position of 0 in both the horizontal and vertical dimensions. Since the horizontal dimension of each grid point is a constant of 3 km, the total horizontal distance from the radar at any grid point is easily calculated. Since the grid points are more tightly packed near the ground than aloft, the elevation in meters of each row had to be read off of the data file in order to calculate the total vertical distance from the radar at any point. The horizontal and vertical distances were used to calculate the slant range, or simply the hypotenuse of the triangle formed. The formula

$$Z = \frac{R^2}{1.7X10^4} + R\sin(\alpha) \tag{4.2}$$

was then used to calculate the elevation angle, α, at each grid point in terms of the height above the ground, Z, and the slant range, R, where Z and R are in km. Eq. 4.2 assumes a standard atmosphere with a vertical refractivity gradient of $-40\ \text{km}^{-1}$.

Attenuation is an extremely important consideration when using millimeter radars due to the increased scattering cross section along the path of the radar beam in the Mie regime. Therefore, one of the important tasks of this modeling study is to determine how detrimental attenuation is to the use of millimeter wavelength radars in observing snowstorms. One output of the T-matrix model is the specific horizontal attenuation in units of dB km^{-1}. However, this is one-way attenuation for one data set. In order to create a radar image, the attenuation needs to be made path dependent. This is done by calculating the exact path from the radar to any grid point. The path calculated reproduced a ray of radar data that was the same width to and from the radar, even though a real radar wave would spread out to make a cone as it progresses from the radar. It is a simpler task, therefore, because the path of the radar wave only passes through one grid point at a time. First, the distance the radar wave traveled as it went through the first grid point from the radar was calculated, and this distance was multiplied by the specific horizontal attenuation given for that grid point. This was done for each grid point along the path. Then, all of the grid points from the radar to the grid point that the calculation was being done for were added together, and this value was multiplied by 2 in order to calculate 2-way attenuation. This total was then subtracted from the value for the original Z_h in dBZ given for the grid point in question, and this Z_h was the actual value a radar would theoretically measure in a snow storm similar to the October 1997 Blizzard. The attenuation proved to be significant at the shorter wavelengths, as discussed in the next section.

4.3 T-matrix Output

A total of 28 plots were generated, with seven plots per wavelength. Each set of plots includes Z_h, path dependent 2-way attenuation, Z_h with attenuation, Z_{dr}, LDR, K_{dp} and ρ_{hv} for each wavelength. These plots represent a grid of 416 grid points, each containing a separate set of calculated radar quantities that are contoured; a hypothetical radar is located on the east side of the plot. They mimic the CSU-CHILL RHI over Fort Collins at about the same time. The same color scale was used in all of the modeled images for a particular radar variable, for example Z_{dr}, over all of the wavelengths for consistency. However, this leads to a rather flat gradient of colors at the extreme wavelengths, S-band and W-band, because to capture the large range of values over all of the wavelengths in one color bar means to confine one wavelength to only part of that color bar. The exception is attenuation, which varies considerably from S-band to W-band; consequently, the scale is changed for Ka and W-band.

4.3.1 Comparison of modeled S-band plots to CHILL

Before an analysis can be done on the modeled images, it is important to compare the modeled S-band images with those of CHILL to determine how well RAMS and T-matrix modeled the actual storm observed by CHILL. Figure 4.3 shows the CHILL RHI's from 25 October 1997 at 0300 UTC, the same time of the modeled images. Figures 4.4 and 4.5 show the RAMS data modeled at S-band. Since Z_h in Figure 4.3a represents the observed Z_h by the "radar", there is no need to include Figures 4.4a and 4.4b, Z_h without attenuation and attenuation, in this comparison. They will be analyzed later to determine the effects of attenuation. Comparing Z_h in Figures 4.3a and 4.4c, the CHILL image spreads out to the west, where the modeled image is about the same depth east to west. This is because the operators of CHILL did not program it to scan all of the way to 90°, whereas the grid used to make the modeled image was a rectangle. There is this difference in all of the images, so the main area of comparison will be directly over Fort Collins, from about 10 to 45 km west of the radar. In both radar images, the highest reflectivities occur near the surface between 30 and 45 km west of the radar. The reflectivities also rapidly diminish above about 2 km AGL. Differences between the two radar images include precipitation intensity and distribution. The RAMS radar image is much more layered, while the CHILL image is cellular east of 30 km from the radar. This is almost certainly due to simplifications and parameterizations, both in T-matrix and RAMS. In modeling with T-matrix, the axis ratio, fall mode, air temperature, and density were fixed. Also, perhaps there is convective precipitation that RAMS did not capture. Concerning intensity, the RAMS image appears to be around 3-5 dBZ too low on average. Overall, though, RAMS put the heaviest precipitation at the right place with similar intensity. Looking at Figures 4.3b and 4.5a, from 0-3 km AGL, Z_{dr}'s in both radar images are mostly between 0 and 1 dB. The exception is above 3 km AGL in the RAMS image, where the Z_{dr} drops to –1 dB. This is probably due to a low signal from the reflectivities that are down to almost –10 dBZ at 4 km AGL (Figure 4.4c). In Figure 4.3a, Z_h is still above zero. This means that the RAMS storm is shallower than what was observed. The Z_{dr}'s close to 0 km in Figure 4.5a are due to the extreme elevation angle of the radar: looking at a slightly oblate snowflake from the bottom makes it appear to lose its slightly horizontal shape. The LDR's shown in Figure 4.3c and 4.5b differs significantly. While LDR's below 2 km AGL are between –29 and –23 dB in the CHILL RHI, those in the RAMS case are much lower, at around –47 dB. A possible explanation is that the LDR's in the CHILL RHI are noisy. Since the entire storm was observed at reflectivities below 35 dBZ, the cross-polar signal is very weak and is probably similar to the noise level in CHILL's receiver. In Figures 4.3d and 4.5c, the values of K_{dp} agree very well. Both of the plots show K_{dp} right around 0 degrees km^{-1}, as expected for this medium. Finally, Figures 4.3e and 4.5d display ρ_{hv}. Both images show values between 0.967 and 0.992, which represents highly correlated precipitation. Overall, the RAMS and T-matrix models seemed to perform well in modeling the October 1997 blizzard. Therefore, an in-depth analysis of the modeled wavelengths can be done with some confidence.

4.3.2 Reflectivity and attenuation

One of the most meaningful calculations in this thesis is that of attenuation and of the effects of attenuation on Z_h at all of the wavelengths. Figures 4.4a, 4.4b, and 4.4c are Z_h without attenuation, total path dependent attenuation (2-way), and Z_h with attenuation factored in, respectively, for S-band. Likewise, Figures 4.6a, 4.6b, and 4.6c are the same plots for Ku-band, Figures 4.8a-c are those plots for Ka-band, and Figures 4.10a-c are for W-band. Z_h without attenuation (at λ's < 10 cm primarily) is a non-physical situation, so these plots serve mainly in assessing the effects of attenuation on Z_h instead of being stand-alone measurements. Also, total path dependent attenuation means that the value shown at a particular location is the total 2-way value for that location: there is no need to sum up the values at each distance along the path to get a total value.

Analyzing the effects of attenuation at S-band is a trivial task, even when the radar is pointed at a thunderstorm (usually). Because snow is a much weaker dielectric than rain (its bulk density is an order of magnitude lower), attenuation is almost non-existent at S-band wavelengths in this case. Since all of the snow aggregates and snow crystals are Rayleigh scatterers at S-band wavelengths, Z_h is not reduced by Mie scattering effects. Also, the scattering cross section, one of the two terms in the extinction cross section, is small. Therefore, little of the incident radiation is lost due to scattering in directions other than back toward the radar. When comparing Figures 4.4a and 4.4c, no discernable difference exists. The attenuation across the entire grid, even through the heavy snow between 30 and 40 km west of the radar near the surface, does not even register 0.01 dB (Figure 4.3b). This means that the Z_h of around 21.01 dBZ around 40 km west of the radar near the surface in Figure 4.4a will be reduced to 21 dBZ in Figure 4.4c. It is clear that attenuation is not a factor at S-band (as expected), and Figure 4.4a could be substituted for Figure 4.4c.

Even though the precipitation still maintains its fundamental structure at Ku-band, the intensity is somewhat diminished (Figure 4.6a). Because the larger snowflakes are within the Mie regime at this wavelength, the backscattering cross section of these hydrometeors is smaller due to increased forward scatter. The heaviest precipitation between 30 and 40 km west of the radar is reduced by 3-5 dBZ. The most attenuated path for the grid, at the surface near -45 km, experiences a total 2-way attenuation of about 0.06 dB (Figure 4.6b). While this is higher than anything at S-band, it still means that the Z_h of 16.06 dBZ at -45 km near the surface in Figure 4.6a will read as 16 dBZ in Figure

4.6c. Again, attenuation, or the extinction cross-section along the path of the radar beam, is not a factor at Ku-band.

At Ka-band, most of the snowflakes and some of the snow crystals are Mie scatterers (Figures 4.8a-c). Z_h is diminished even more to a maximum of less than 11 dBZ due to the larger forward scattering cross sections of the Mie scatterers (Figure 4.8). Effectively, the actual radar signal is much weaker, as the reflectivity is 15 dBZ lower at the peak value when compared to S-band (Figure 4.4a). The scale of attenuation has been changed to account for the drastic increase at Ka-band (Figure 4.8b). Instead of spanning from 0 to 0.1 dBZ like it did at S and Ku-band, the scale now spans from 0 to 10 dB. In fact, the total attenuation at –45 km near the surface is now about 2.5 dB, much larger than the attenuation at this same point in S-band. The Z_h at –45 km near the surface of 10 dBZ in Figure 4.8a would be reduced to 7.5 dBZ in Figure 4.8c.

Every grid point at W-band registers Z_h below 0 dBZ (Figure 4.10a). The significant snowstorm, as it appeared at S-band, is now reduced to two color contours of negative Z_h. The entire storm is now deeply in the Mie regime, and the very low signal caused by the large forward scattering cross section of the snow aggregates and crystals and the oscillatory nature of the backscattering cross section will likely make the measurements of the other polarimetric radar quantities difficult to interpret. While Z_h values of precipitation spanned from 0-25 dBZ or higher at S-band, the span is only –10 to 0 dBZ at W-band. Attenuation is severe, with values as high as 10 dB or higher at –45 km near the surface (Figure 4.10b). Comparing Figure 4.10b to Figure 4.4b, the total attenuation is 10 dB at W-band at -45 km near the surface and is 0.01 dB at most at S-band for the same path. Hence, the total attenuation for this location in the "storm" is an order of magnitude higher (in linear units) at W-band then at S-band. The effects of different paths taken by the radar beam is shown very clearly when comparing Figures 4.10a and 4.10b. Even though the point at 8 km AGL above –45 km represents the longest path, the attenuation is more severe at this range near the ground because the slightly shorter path goes through the highest reflectivities for the longest period of time. The magnitude of the attenuation at most locations on the grid has detrimental effects on the actual radar observed Z_h (Figure 4.10c). Most of the reflectivities are around -10 dBZ or lower, and this would not be a useful image to work with while observing an actual snowstorm. Most of the incident radiation has been scattered in directions away from the radar and lost on its attempted round trip through the storm, returning as a very low signal to the "radar".

4.3.3 Polarimetric measurements

Figures 4.5a-d are plots of Z_{dr}, LDR, K_{dp}, and ρ_{hv}, respectively, at S-band. Figures 4.7a-d are the same plots at Ku-band, Figures 4.9a-d are these plots at Ka-band, and Figures 4.11a-d are these plots at W-band. Before the analysis, it should be stated that the complex patterns of the plots and apparent holes in the color scale in the RAMS images that begin above the precipitation represent clear air or clouds: in the CHILL images, these values were filtered out as the result of a low signal to noise ratio. The "top" of the precipitation loosely correlates to a value of around 0 dBZ at S-band, although this isn't the same at the other wavelengths due to signal reduction. For the purposes of this study, these areas above the precipitation should be ignored. These areas correspond to around 3 km AGL and up at all of the wavelengths.

The Z_{dr} values in Figure 4.5a between 0 and 1 dB are typical of dry snow at S-band (Lhermitte, 2002). The reductions in Z_{dr} above 2 km AGL and at 0 km range and the LDR values (Figure 4.5b) were addressed in the comparison of the modeled S-band wavelengths and CHILL images. Lhermitte (2002) shows that K_{dp} values of around 0 degrees km^{-1} are expected for dry snow at S-band (Figure 4.5c). The area of slightly higher K_{dp} between –10 and –20 km at 3.5 km AGL could be an area of high snow crystal concentration with a preferred orientation or "wet" snow, resulting in some phase shift. These higher values reflect the horizontal nature of dendrites, which tend to have a larger phase shift in the horizontal than in the vertical. The ρ_{hv} values in Figure 4.5d very close to unity are also typical of dry snow (Lhermitte, 2002).

The Z_{dr}, LDR, and ρ_{hv} values at Ku-band are very similar to those modeled at S-band (Figures 4.7a-b, Figure 4.7d). At Ku-band, the K_{dp} values in Figure 4.7c have increased and reveal a much more complex distribution when compared to S-band. The increase in K_{dp} with frequency is validated quantitatively in Bringi and Chandrasekar (2001) down to 35 GHz.

At Ka-band, the Z_{dr} and ρ_{hv} values are close to the same values that they were for S and Ku-band (Figures 4.9a and 4.9d). The LDR has somewhat increased in some of the area below 3 km AGL, however (Figure 4.9b). The same pattern is evident in Table 3.6, where the LDR values are slightly higher for snow aggregates in Ka-band relative to S and Ku-band. The K_{dp} plot at Ka-band is very similar in structure to the Ku-band plot, but the values are higher and more difficult to interpret (Figure 4.9c).

The plots at W-band reveal strong Mie scattering effects, specifically strong forward scattering causing a reduction in Z_h and oscillatory backscattering behavior.

Although the Z_{dr} values in Figure 4.11a are similar in value to the other wavelengths, the higher values between –30 and –40 km near the surface correspond to values of LDR, K_{dp}, and ρ_{hv} that are difficult to interpret (Figures 4.11b-d). The LDR values of close to 0 dB at this location are very different when compared to S-band; a cross-polar signal the same strength as a co-polar signal shows that LDR is undeterminable, in a sense, at this wavelength. This area corresponds to the area where the most intense snowfall was (Figure 4.4a), and the greater number of hydrometeors and sizes can create ambiguity (in an observational sense) in the calculations of the radar variables due to strong Mie effects. In fact, this is what is seen in Figures 4.11b-d. There is no discernable pattern for K_{dp} values in Figure 4.11c, and ρ_{hv} drops to around 0.5 in the area mentioned above.

It is clear from this analysis that Z_h and the other polarimetric variables at W-band and possibly Ka-band are severely diminished and difficult to interpret at times. This is due to Mie scattering effects, in which forward scattering is greatly increased from that of the Rayleigh regime and backscattering is oscillatory. Also, W-band experiences severe attenuation, even by dry snow. Little physical interpretation can be done for all of the W-band plots and some of the Ka-band plots, at least for these intense snowstorms at significant ranges.

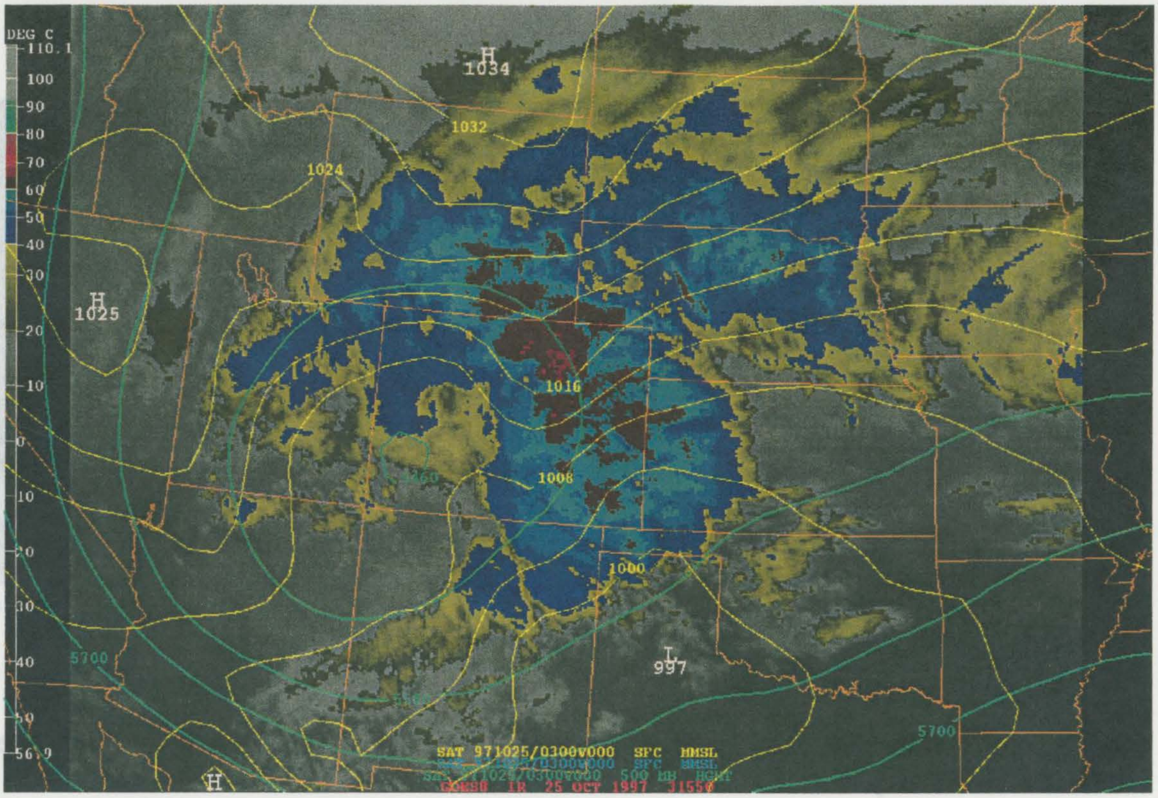

Figure 4.1: Infrared satellite picture for 0300 UTC on 25 October 1997 from the NWS (URL: http://www.crh.noaa.gov/pub/blizzard97/images/24oct500sfc6.gif, 2003).

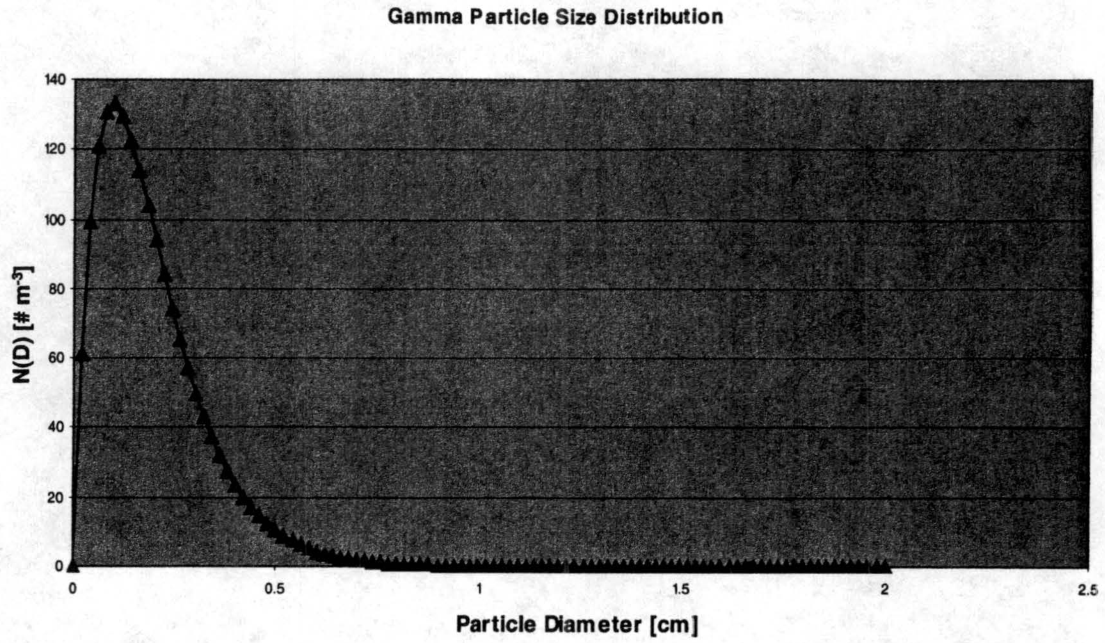

Figure 4.2: One of several hundred gamma distributions for snow aggregates used in this case study.

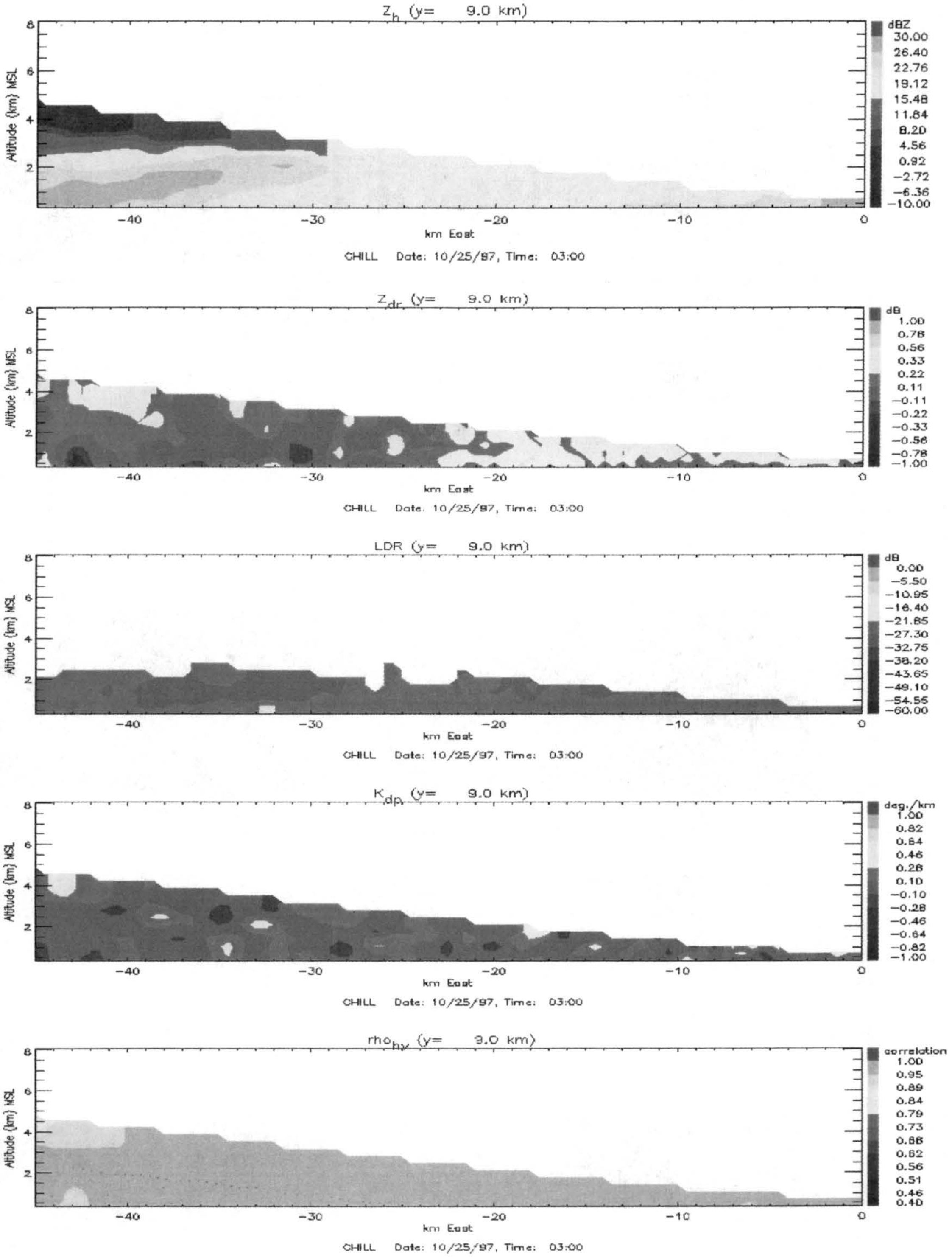

Figure 4.3: CHILL RHI for 0300 UTC on 25 October 1997 measuring (a) Z_h, (b) Z_{dr}, (c) LDR, (d) K_{dp} and (e) ρ_{hv}.

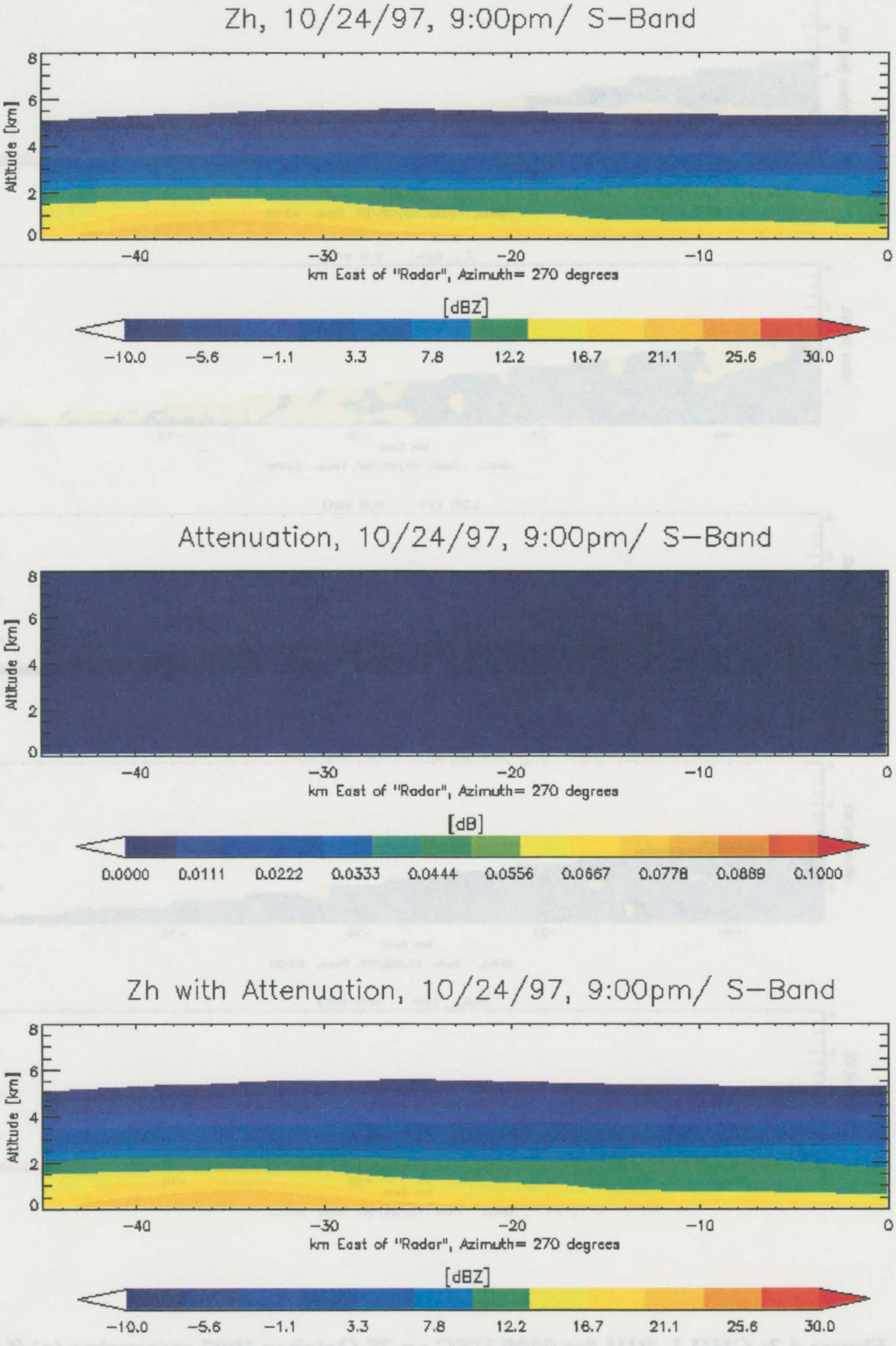

Figure 4.4: RAMS data modeled at S-band for 0300 UTC on 25 October 1997: (a) Z_h, (b) attenuation and (c) attenuated (observed) Z_h.

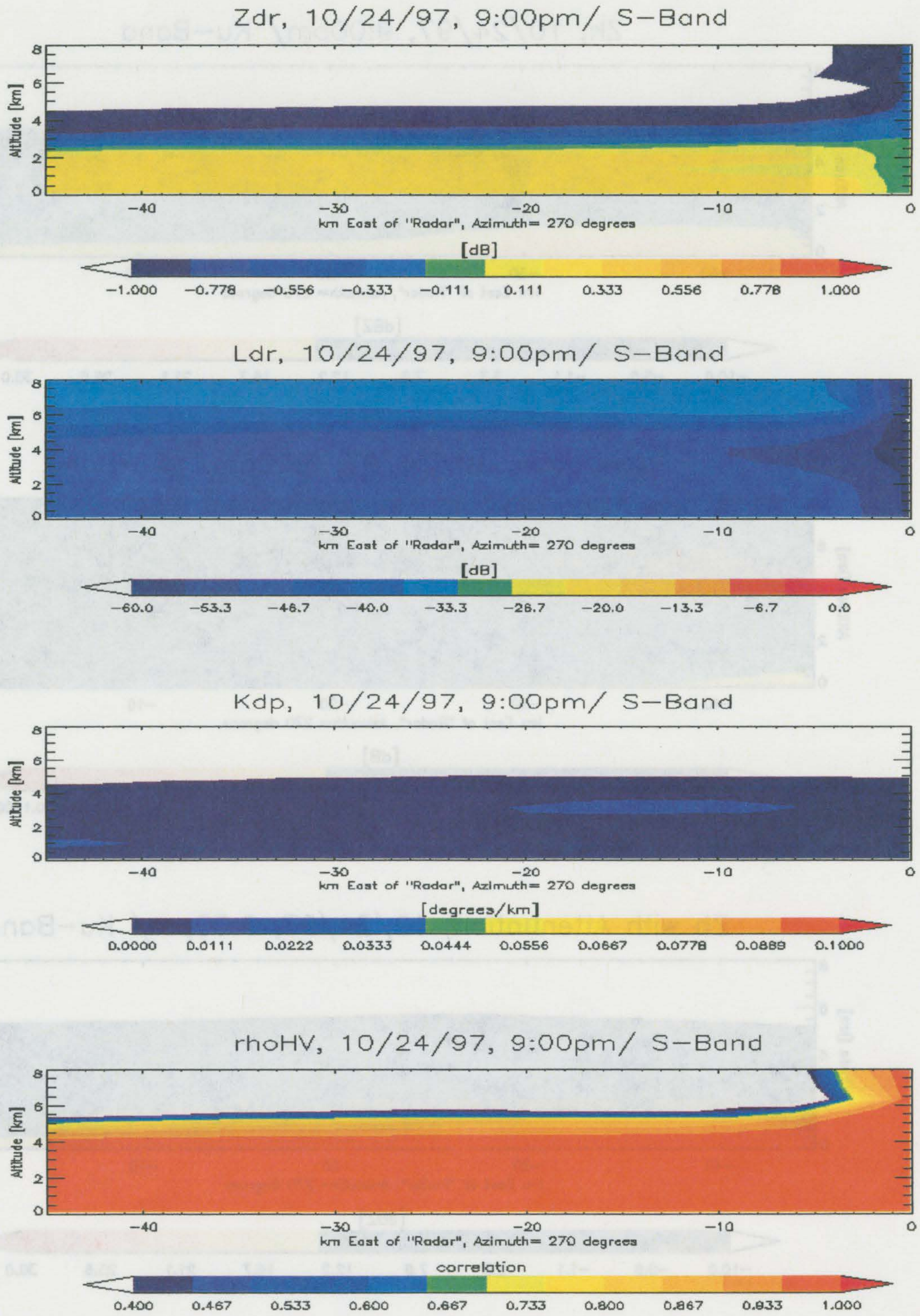

Figure 4.5: RAMS data modeled at S-band for 0300 UTC on 25 October 1997: (a) Z_{dr}, (b) LDR, (c) K_{dp} and (d) ρ_{hv}.

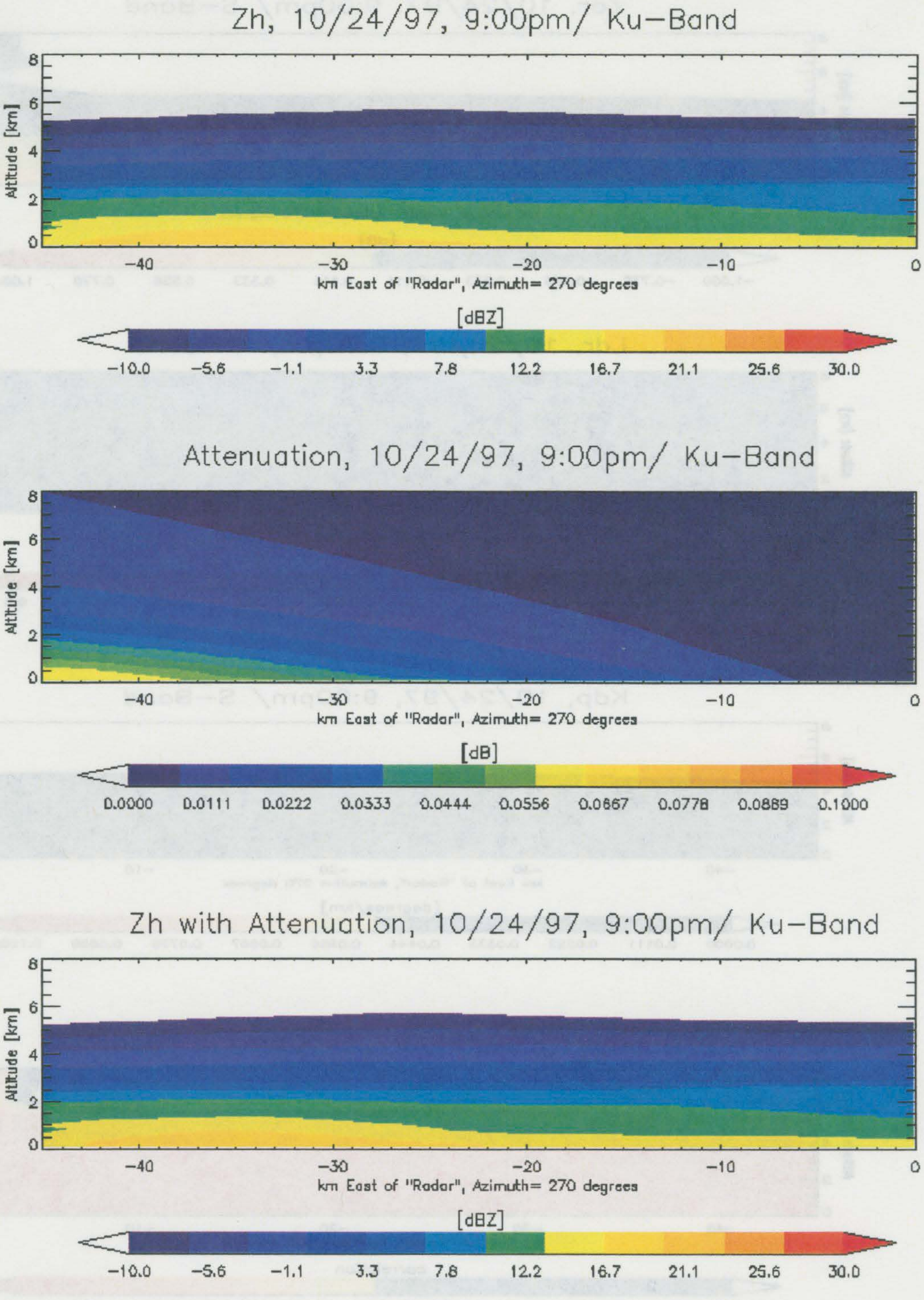

Figure 4.6: RAMS data modeled at Ku-band for 0300 UTC on 25 October 1997: (a) Z_h, (b) attenuation and (c) attenuated (observed) Z_h.

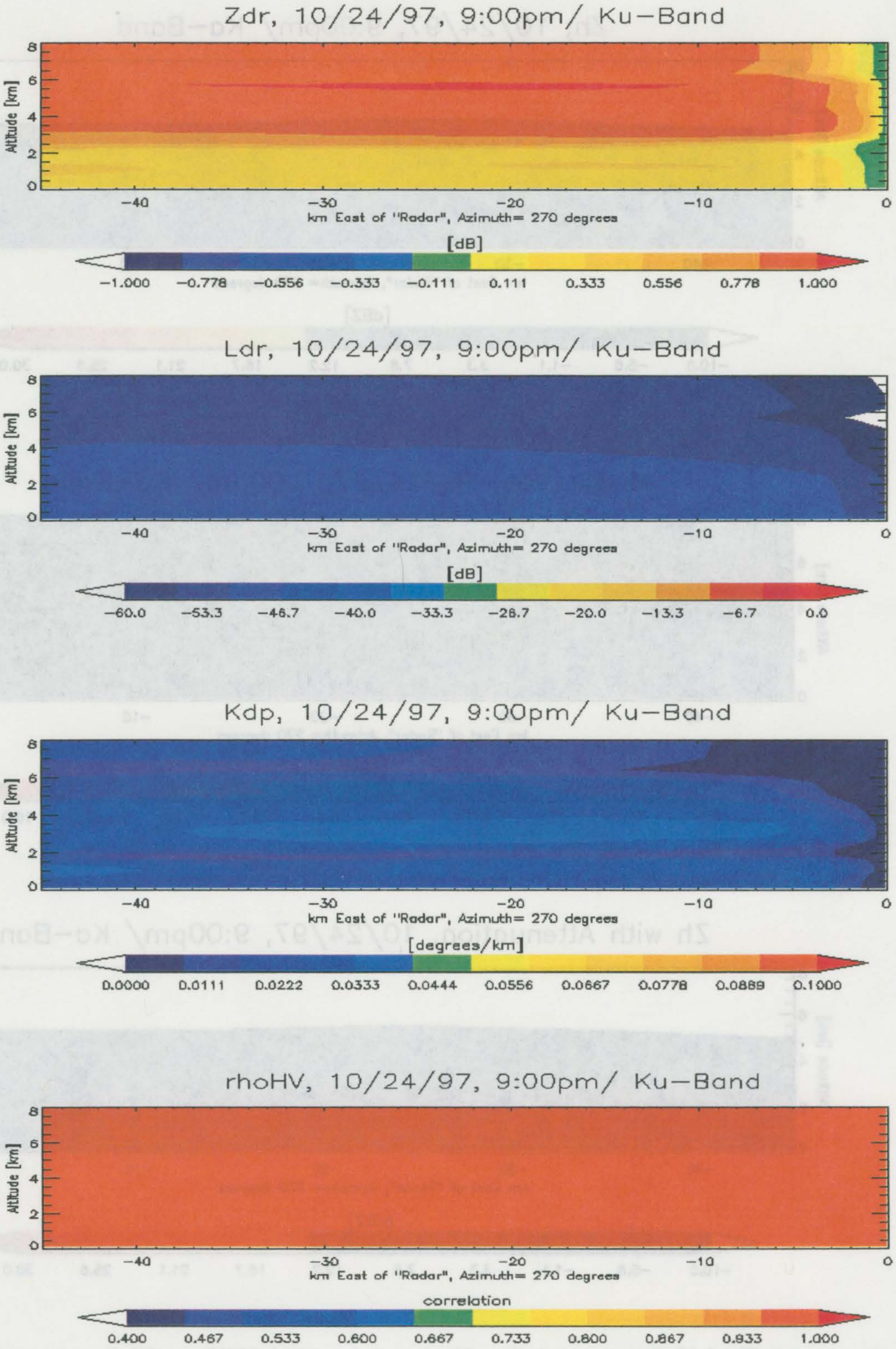

Figure 4.7: RAMS data modeled at Ku-band for 0300 UTC on 25 October 1997: (a) Z_{dr}, (b) LDR, (c) K_{dp} and (d) ρ_{hv}.

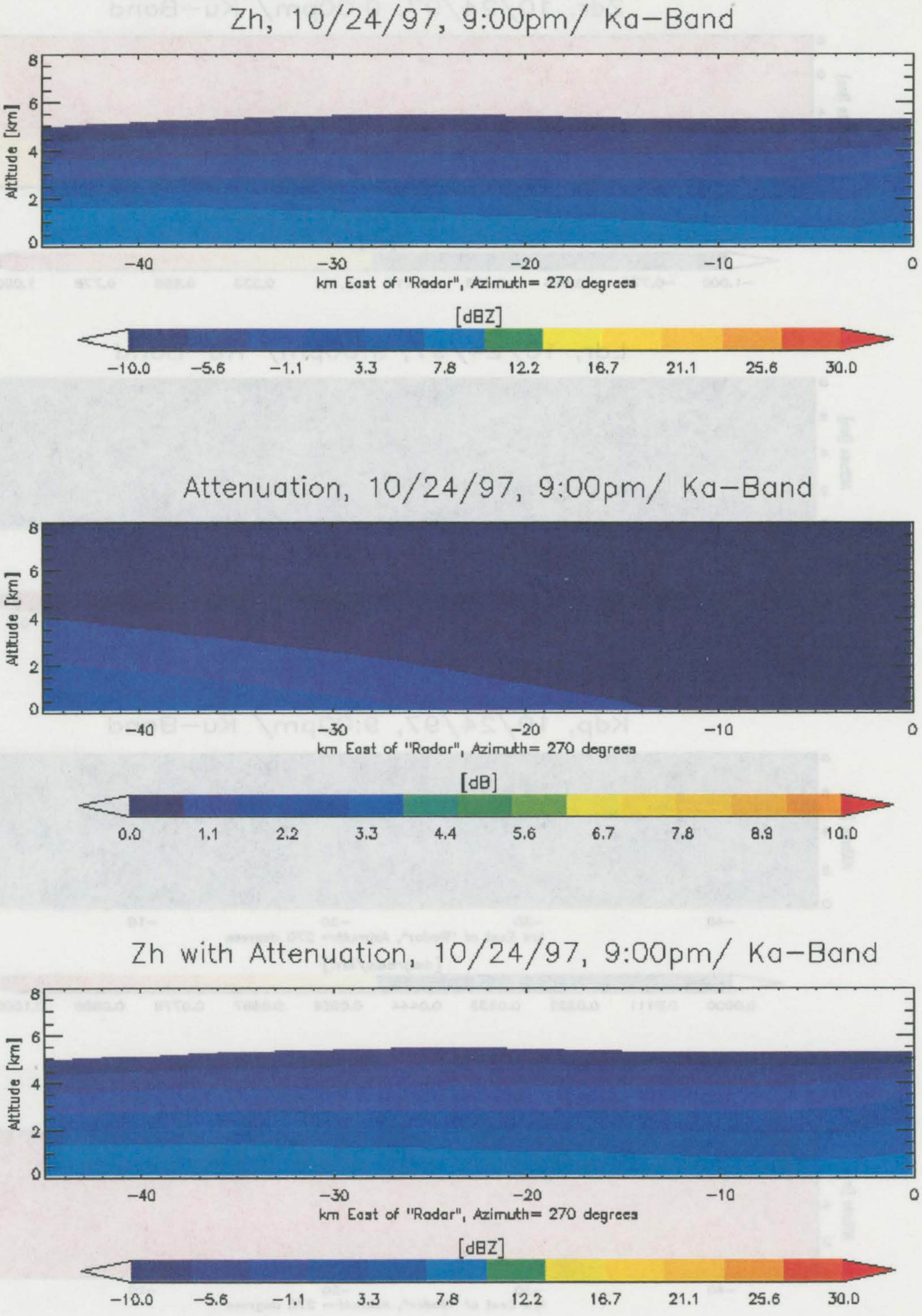

Figure 4.8: RAMS data modeled at Ka-band for 0300 UTC on 25 October 1997: (a) Z_h, (b) attenuation and (c) attenuated (observed) Z_h.

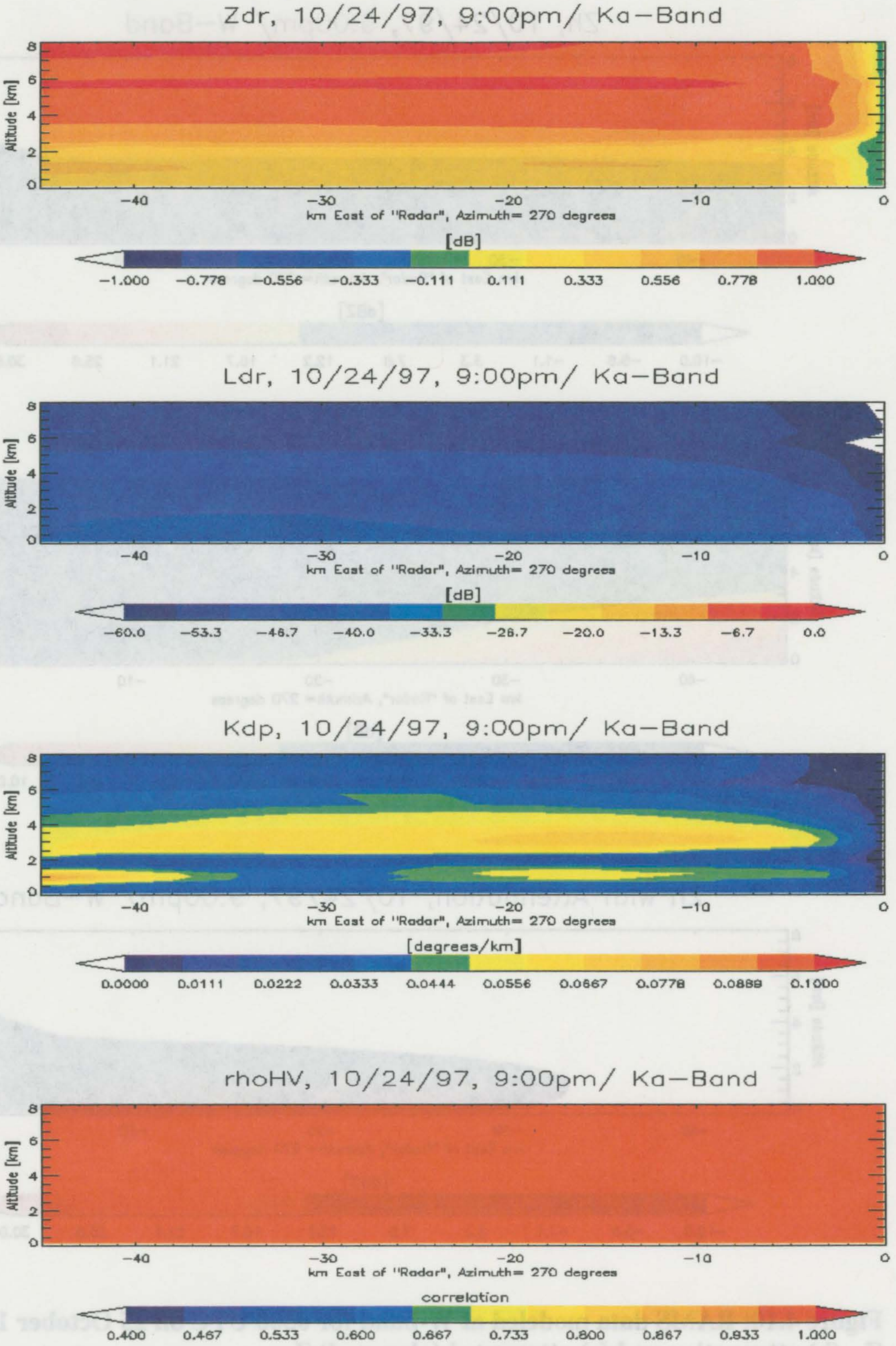

Figure 4.9: RAMS data modeled at Ka-band for 0300 UTC on 25 October 1997: (a) Z_{dr}, (b) LDR, (c) K_{dp} and (d) ρ_{hv}.

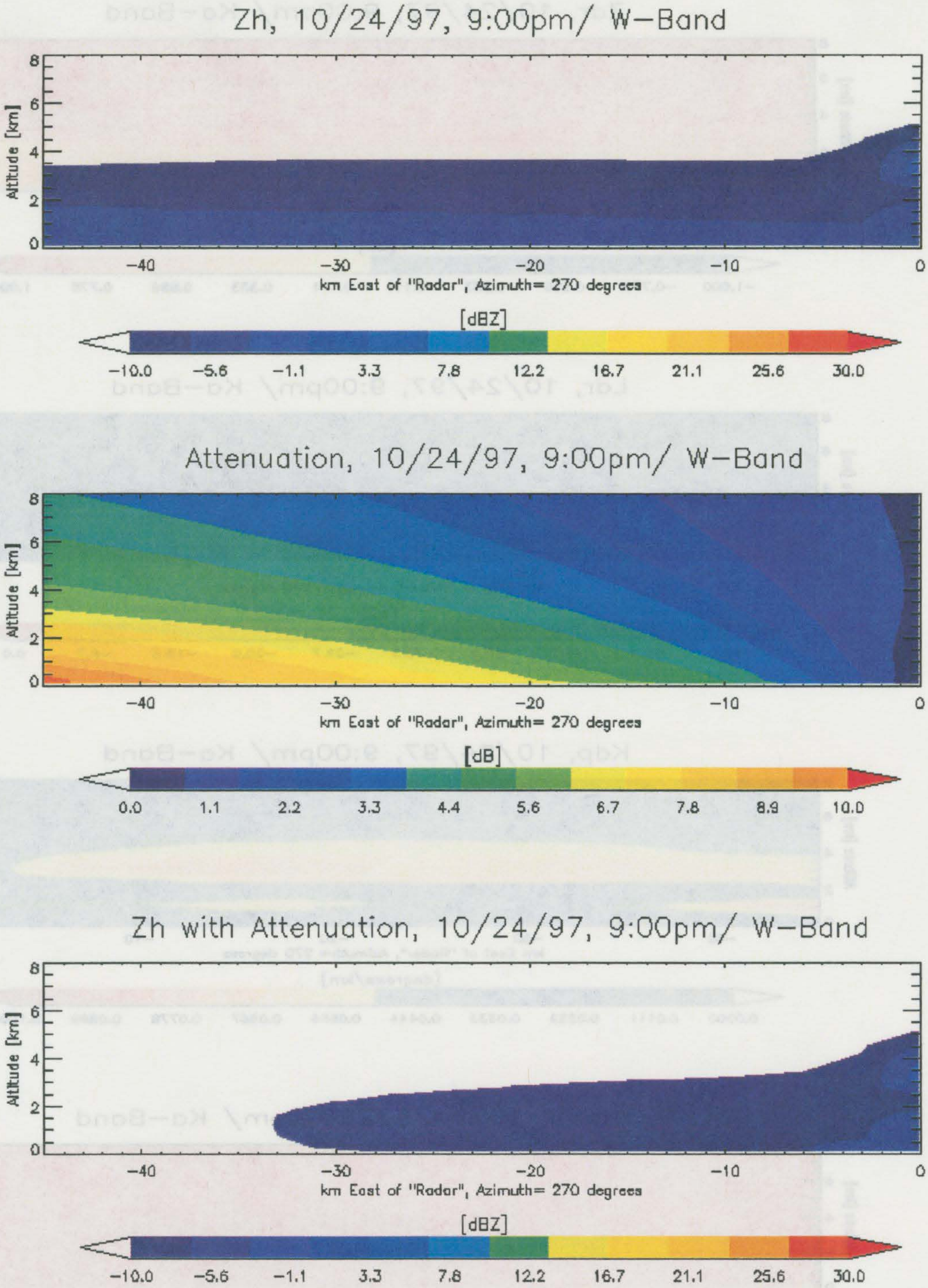

Figure 4.10: RAMS data modeled at W-band for 0300 UTC on 25 October 1997: (a) Z_h, (b) attenuation and (c) attenuated (observed) Z_h.

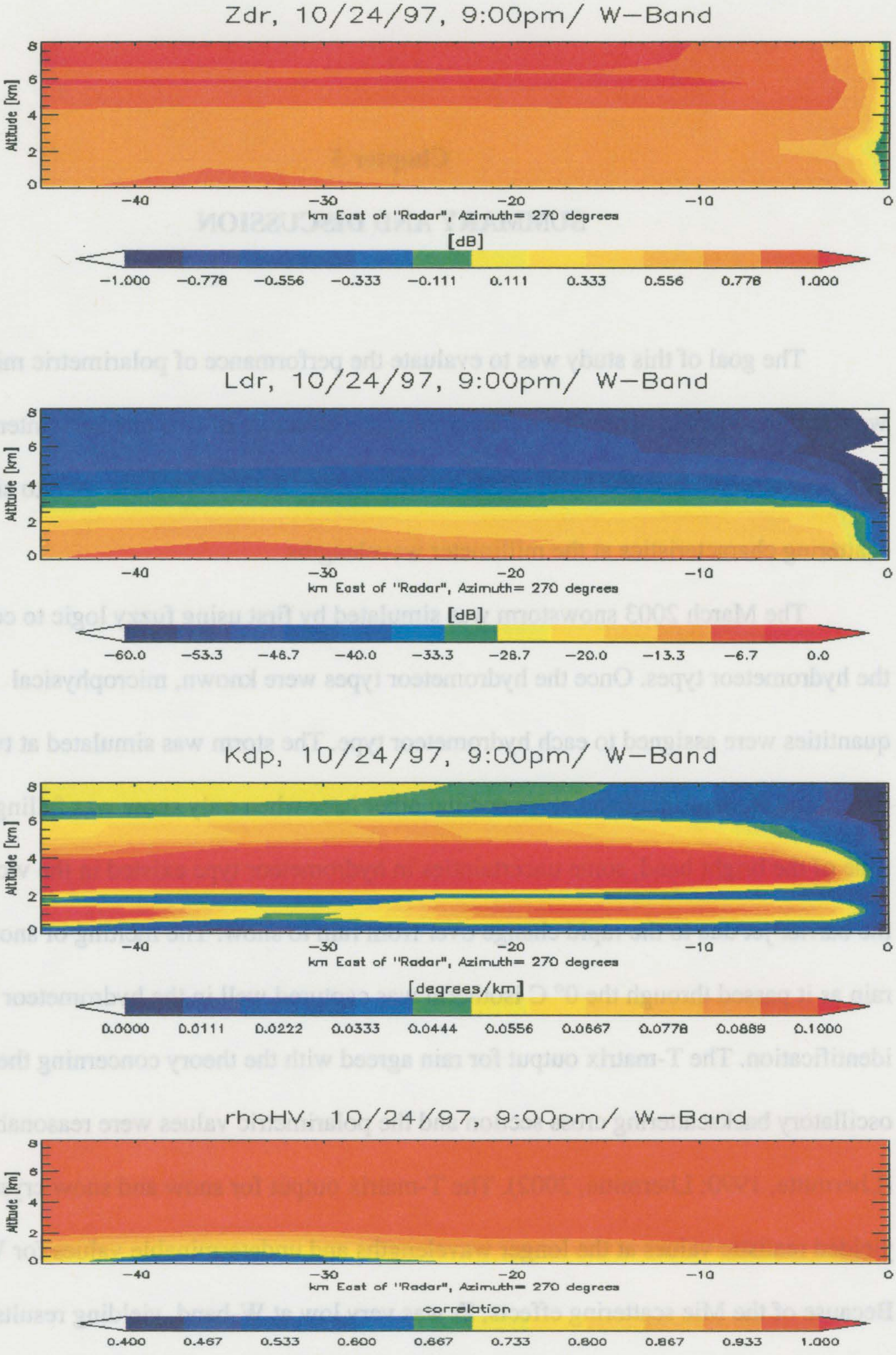

Figure 4.11: RAMS data modeled at W-band for 0300 UTC on 25 October 1997: (a) Z_{dr}, (b) LDR, (c) K_{dp} and (d) ρ_{hv}.

Chapter 5

SUMMARY AND DISCUSSION

The goal of this study was to evaluate the performance of polarimetric millimeter wavelength radars in observing the microphysical structure of two intense winter storms. The storms were observed by the CSU-CHILL radar. CHILL data were used to simulate scattering characteristics at the millimeter wavelengths.

The March 2003 snowstorm was simulated by first using fuzzy logic to constrain the hydrometeor types. Once the hydrometeor types were known, microphysical quantities were assigned to each hydrometeor type. The storm was simulated at two times, one at the bright band stage and the other later when only snow was falling. At the time of the bright band, some uncertainties in hydrometeor type existed in the vicinity of the barrier jet due to the rapid change over from rain to snow. The melting of snow into rain as it passed through the 0° C isotherm was captured well in the hydrometeor identification. The T-matrix output for rain agreed with the theory concerning the oscillatory backscattering cross section and the polarimetric values were reasonable (Lhermitte, 1990; Lhermitte, 2002). The T-matrix output for snow and snow crystals yielded realistic values at the longer wavelengths and undeterminable values for W-band. Because of the Mie scattering effects, Z_h was very low at W-band, yielding results that were difficult to interpret for the other polarimetric quantities. Changing the density of the snow aggregates and crystals also greatly affected the output. It is apparent that the snow aggregate and crystal density is not exactly known, and even small changes can greatly effect Z_h. Trends that were consistent throughout this case were that attenuation increased as wavelength decreased, and attenuation was greater for rain than for snow aggregates and snow crystals. Also, Mie scattering effects generally decreased Z_h at shorter wavelengths.

RAMS was used to assign the microphysical information concerning the October 1997 blizzard in order to model it using T-matrix. The RAMS model was initialized and was run at the same time as the observed storm. A grid was created to accommodate the amount of microphysical information supplied by RAMS. The T-matrix model was then applied at each grid point in order to output contoured modeled radar images. In order to test the performance of RAMS, the modeled S-band output was compared to the observations made by CHILL. In general, the modeled images at S and Ku-bands were easily interpreted concerning the structure of the storm and the values of the polarimetric variables (Lhermitte, 2002). However, at Ka and especially W-band, both the values of the polarimetric variables and the structure of the image were difficult to interpret. While attenuation was very small at S and Ku-band, it was more detectable at Ka-band and obvious at W-band as it changed the structure of the radar image by "erasing" the back part of the storm. It should be mentioned that contrary to this study, in cases with all rain it is possible to reconstruct the unattenuated reflectivity field by using ϕ_{dp} (Bringi and Chandrasekar, 2001). In addition to severe attenuation, due to Mie scattering effects, Z_h was greatly reduced to below 0 dBZ at all points in the radar image at W-band. This, along with the oscillatory nature of the Mie regime, yielded results of the other polarimetric quantities that were undeterminable at W-band. The effects were not as severe at Ka-band.

Because the snow was deep in the Mie regime at Ka-band and especially W-band, Mie effects (increased forward scatter and oscillatory backscattering behavior) greatly reduced Z_h at these wavelengths, making the data difficult to interpret. From this study, it is concluded that, with regard to intense snowstorms observed at significant ranges and millimeter wavelengths (especially W-band):

- Strong Mie scattering renders the polarimetric quantities difficult to interpret, and
- Attenuation is severe, causing significant signal loss.

Because of this, W-band and possibly Ka-band may have limited use in observing *intense* winter storms, at least at significant ranges. However, as mentioned in Chapter 2, W-band is a sensitive cloud radar wavelength and is widely used in the field of atmospheric science. W-band is the radar of choice on the CloudSat radar (Stephens et al., 2002). Also, a W-band system is currently being used to probe weak storms and cirrus clouds at great detail on board the U. of Wyoming King Air aircraft. For dual-wavelength radar applications, such as calculating snowfall rates and for observational purposes, Ku-band appears to be useful in studying winter storms of this magnitude. Ku-band would offer an economical advantage over S-band in observing snowstorms with its smaller antenna and less powerful transmitter. Also, Ku-band is more portable, and could more easily be moved to a more favorable location for observation.

This study advances our understanding of millimeter wavelength radars with respect to their performance in observing major winter storms. This modeling study can be used as a stepping-stone in evaluating the operational performance of the University of Massachusetts' AMFR in observing winter storms. Also, more detailed modeling could be done to determine the sensitivity of the polarimetric variables to different hydrometeors and particle size distributions at each wavelength.

REFERENCES

Barber, P., and C. Yeh, 1975: Scattering of electromagnetic waves by arbitrarily shaped dielectric bodies. *Appl. Opt.*, **14**, 2864-2872.

Barthazy, E., and R. Schefold, 2003: Properties of snowflakes of different riming degree and crystal types. Preprints, *31st Conf. on Radar Meteorology*, Seattle, WA, Amer. Meteor. Soc., 124-127.

Battan, L. J., 1973: Radar Observation of the Atmosphere, The University of Chicago Press, Chicago, Illinois, 324 pp.

Beard, K. V., and A. R. Jameson, 1983: Raindrop canting. *J. Atmos. Sci.*, **40**, 448-454.

Bierly, G. D., and J. A. Winkler, 2001: A composite analysis of airstreams within cold-season Colorado cyclones. *Wea. Forecasting*, **16**, 57-80.

Bringi, V. N., and V. Chandrasekar, 2001: Polarimetric Doppler Weather Radar-Principals and Applications, Cambridge University Press, Cambridge, UK, 656 pp.

Carey, L. Personal communication on the T-matrix model, 2003.

Clark, J. H. E., 1990: An observational and theoretical study of Colorado lee cyclogenesis. *J. Atmos. Sci.*, **47**, 1541-1561.

Doviak, R. J., and D. S. Zrnic, 1993: Doppler Radar and Weather Observations, 2nd Ed., Academic Press, San Diego, California, 562 pp.

Dunn, L. B., 1987: Cold air damming by the Front Range of the Colorado Rockies and its relationship to locally heavy snows. *Wea. Forecasting*, **2**, 177-189.

Dunn, L. B., 1988: Vertical motion evaluation of a Colorado snowstorm from a synoptician's perspective. *Wea. Forecasting*, **3**, 261-272.

Fabry, F., and I. Zawadzki, 1995: Long-Term radar observations of the melting layer of precipitation and their interpretation. *J. Atmos. Sci.*, **52**, 838-851.

Galloway, J., A. Pazmany, J. Mead, R. E. McIntosh, D. Leon, J. French, R. Kelly, and G. Vali, 1997: Detection of ice hydrometeor alignment using an airborne W-band polarimetric radar. *J. Atmos. Oceanic Technol.*, **14**, 3-12.

Herzegh, P. H., and A. R. Jameson, 1992: Observing precipitation through dual-polarization radar measurements. *Bull. Amer. Meteor. Soc.*, **73**, 1365-1374.

Heymsfield, A., 1972: Ice crystal terminal velocities. *J. Atmos. Sci.*, **29**, 1348-1357.

Heymsfield, A. J., A. Bansemer, P. R. Field, S. L. Durden, J. L. Stith, J. E. Dye, W. Hall, and C. A. Grainger, 2002: Observations and parameterizations of particle size distributions in deep tropical cirrus and stratiform precipitating clouds: Results from in situ observations in TRMM field campaigns. *J. Atmos. Sci.*, **59**, 3457-3491.

Heymsfield, A. J. Personal communication on the density of snow aggregates and crystals based on studies not yet published, 2003.

Jameson, A. R., 1983: Microphysical interpretation of multi-parameter radar measurements in rain. Part I: Interpretation of polarization measurements and estimation of raindrop shapes. *J. Atmos. Sci.*, **40**, 1792-1802.

Lhermitte, R., 1990: Attenuation and scattering of millimeter wavelength radiation by clouds and precipitation. *J. Atmos. Oceanic Technol.*, **7**, 464-479.

Lhermitte, R., 2002: Centimeter and Millimeter Wavelength Radars in Meteorology, Lhermitte Publications, Miami, Florida, 550 pp.

Liu, H., and V. Chandrasekar, 2000: Classification of hydrometeors based on polarimetric radar measurements: Development of fuzzy logic and neuro-fuzzy systems, and in situ verification. *J. Atmos. Oceanic Technol.*, **17**, 140-162.

Locatelli, J. D., and P. V. Hobbs, 1974: Fall speeds and masses of solid precipitation particles. *J. Geophys. Res.*, **79**, 2185-2197.

Lo, K. K., and R. E. Passarelli, 1982: The growth of snow in winter storms: An airborne observational study. *J. Atmos. Sci.*, **39**, 697-706.

Marshall, J. S., and W. McK. Palmer, 1948: The distribution of raindrops with size. *J. Meteor.*, **5**, 165-166.

Marwitz, J., and J. Toth, 1993: The Front Range Blizzard of 1990. Part I: Synoptic and mesoscale structure. *Mon. Wea. Rev.*, **121**, 402-415.

Matrosov, S. Y., 1998: A dual-wavelength radar method to measure snowfall rate. *J. Appl. Meteor.*, **37**, 1510-1521.

Matrosov, S. Y., R. F. Reinking, R. A. Kropfli, and B. W. Bartram, 1996: Estimation of ice hydrometeor types and shapes from radar polarization measurements. *J. Atmos. Oceanic Technol.*, **13**, 85-96.

Meyers, P. M., R. L. Walko, J. Y. Harrington, and W. R. Cotton, 1997: New RAMS cloud microphysics parameterization. Part II: The two-moment scheme. *Atmos. Res.*, **45**, 3-39.

Nakamura, K., and H. Inomata, 1991: Non-Rayleigh scattering effect in rain observations by an X- and Ka-band dual-wavelength radar. *J. Atmos. Oceanic Technol.*, **8**, 352-362.

Passarelli, R. E., 1978: An approximate analytical model of the vapor deposition and aggregation growth of snowflakes. *J. Atmos. Sci.*, **35**, 118-124.

Passarelli, R. E., and R. C. Srivastava, 1979: A new aspect of snowflake aggregation theory. *J. Atmos. Sci.*, **36**, 484-493.

Passarelli, R. E., 1978: Theoretical and observational study of snow-size spectra and snowflake aggregation efficiencies. *J. Atmos. Sci.*, **35**, 882-889.

Politovich, M. K., and B. C. Bernstein, 1995: Production and depletion of supercooled liquid water in a Colorado winter storm. *J. Appl. Meteor.*, **34**, 2631-2648.

Pruppacher, H. R., and J. D. Klett, 1997: Microphysics of Clouds and Precipitation, 2nd Ed., Kluwer Academic Publishers, Dordrecht, The Netherlands, 954 pp.

Rinehart, R. E., 1997: Radar for Meteorologists, Rinehart Publications, Grand Forks, North Dakota, 428 pp.

Rutledge, S. A., and P. V. Hobbs, 1983: The mesoscale and microscale structure and organization of clouds and precipitation in midlatitude cyclones. VIII: A model for the "Seeder-Feeder" process in warm-frontal rainbands. *J. Atmos. Sci.*, **40**, 1185-1206.

Ryan, B. F., 2000: A bulk parameterization of the ice particle size distribution and the optical properties in ice clouds. *J. Atmos. Sci.*, **57**, 1436-1451.

Ryzhkov, A. V., and D. S. Zrnic, 1998: Discrimination between rain and snow with a polarimetric radar. *J. Appl. Meteor.*, **37**, 1228-1240.

Smith, P. L., 1984: Equivalent radar reflectivity factors for snow and ice particles. *J. Climate Appl. Meteor.*, **23**, 1258-1260.

Stephens, G. L., D. G. Vane, R. J. Boain, G. G. Mace, K. Sassen, Z. Wang, A. J. Illingworth, E. J. O'Connor, W. B. Rossow, S. L. Durden, S. D. Miller, R. T. Austin, A. Benedetti, C. Mitrescu, and the CloudSat Science Team, 2002: The CloudSat mission and the A-Train: a new dimension of space-based observations of clouds and precipitation. *Bull. Amer. Meteor. Soc.*, **83**, 1771-1790.

Stewart, R. E., J. D. Marwitz, and J. C. Pace, 1984: Characteristics through the melting layer of stratiform clouds. *J. Atmos. Sci.*, **41**, 3227-3237.

Straka, J. M., D. S. Zrnic, and A. V. Ryzhkov, 2000: Bulk hydrometeor classification and quantification using polarimetric radar data: Synthesis of relations. *J. Appl. Meteor.*, **39**, 1341-1372.

Ulbrich, C. W., 1983: Natural variations in the analytical form of the raindrop size distribution. *J. Climate Appl. Meteor.*, **22**, 1764-1775.

Vivekanandan, J., D. S. Zrnic, S. M. Ellis, R. Oye, A. V. Ryzhkov, and J. Straka, 1999: Cloud microphysics retrieval using S-band dual-polarization radar measurements. *Bull. Amer. Meteor. Soc.*, **80**, 381-388.

Vivekanandan, J., W. M. Adams, and V. N. Bringi, 1991: Rigorous approach to polarimetric radar modeling of hydrometeor orientation distributions. *J. Appl. Meteor.*, **30**, 1053-1063.

Walko, R. L., W. R. Cotton, M. P. Meyers, and J. Y. Harrington, 1995: New RAMS cloud microphysics parameterization Part I: The single-moment scheme. *Atmos. Res.*, **38**, 29-62.

Zrnic, D. S., N. Balakrishnan, C. L. Ziegler, V. N. Bringi, K. Aydin, and T. Matejka, 1993b: Polarimetric signatures in the stratiform region of a mesoscale convective system. *J. Appl. Meteor.*, **32**, 678-693.